Original Paper

Experimental study of the effects of a multistage pore-throat structure on the seepage characteristics of sandstones in the Beibuwan Basin: Insights into the flooding mode

Lei Wang [a, b, *], Xiao Lei [a], Qiao-Liang Zhang [a], Guang-Qing Yao [b], Bo Sui [a], Xiao-Jun Chen [c, d, **], Ming-Wei Wang [a], Zhen-Yu Zhou [a], Pan-Rong Wang [e], Xiao-Dong Peng [e]

[a] *Zhanjiang Branch, China National Offshore Oil Corporation (CNOOC) Limited, Zhanjiang, 524057, Guangdong, China*
[b] *Faculty of Earth Resources, China University of Geosciences (Wuhan), Wuhan, 430074, Hubei, China*
[c] *School of Resources and Safety Engineering, Chongqing University, Chongqing, 400044, China*
[d] *School of Engineering, University of Manchester, Manchester M13 9WJ, UK*
[e] *Hainan Branch, China National Offshore Oil Corporation (CNOOC) Limited, Haikou, 570311, Hainan, China*

ARTICLE INFO

ABSTRACT

To investigate the relationship between grain sizes, seepage capacity, and oil-displacement efficiency in the Liushagang Formation of the Beibuwan Basin, this study identifies the multistage pore-throat structure as a crucial factor through a comparison of oil displacement in microscopic pore-throat experiments. The two-phase flow evaluation method based on the Li−Horne model is utilized to effectively characterize and quantify the seepage characteristics of different reservoirs, closely relating them to the distribution of microscopic pores and throats. It is observed that conglomerate sandstones at different stages exhibit significant heterogeneity and noticeable differences in seepage capacity, highlighting the crucial role played by certain large pore throats in determining seepage capacity and oil displacement efficiency. Furthermore, it was found that the displacement effects of conglomeratic sandstones with strong heterogeneity were inferior to those of conventional homogeneous sandstone, as evidenced by multiple displacement experiments conducted on core samples with varying granularities and flooding systems. Subsequently, core-based experiments on associated gas flooding after water flooding were conducted to address the challenge of achieving satisfactory results in a single displacement mode for reservoirs with significant heterogeneity. The results indicate that the oil recovery rates for associated gas flooding after water flooding increased by 7.3%−16.4% compared with water flooding alone at a gas−oil ratio of approximately 7000 m^3/m^3. Therefore, considering the advantages of gas flooding in terms of seepage capacity, oil exchange ratio, and the potential for two-phase production, gas flooding is recommended as an energy supplement mode for homogeneous reservoirs in the presence of sufficient gas source and appropriate tectonic angle. On the other hand, associated gas flooding after water flooding is suggested to achieve a more favorable development effect compared to a single mode of energy supplementation for strongly heterogeneous sandstone reservoirs.

1. Introduction

The Beibuwan (BBW) Basin holds significant proven reserves, accounting for 76% of the reserves and 70% of the oil production in the oilfields located in the western South China Sea (Jiang et al., 2021). The Liushagang (LSG) Formation, which is the focus of this study, serves as the primary production layer in the BBW oilfield.

* Corresponding author. Zhanjiang Branch, China National Offshore Oil Corporation (CNOOC) Limited, Zhanjiang, 524057, Guangdong, China.
** Corresponding author. School of Resources and Safety Engineering, Chongqing University, Chongqing, 400044, China.
E-mail addresses: wang_lei@cug.edu.cn (L. Wang), chenxiaojuncug@hotmail.com (X.-J. Chen).

The reservoirs within the LSG Formation exhibit notable differences in granularity, strong heterogeneity of pore structures, and complex fault structures. Currently, the production process primarily adopts the single water flooding development mode. However, it has been proven that there are significant variations in seepage capacity and oil-displacement efficiency among different pore-throat structures (Jiang et al., 2021). To effectively exploit the reservoirs with immense potential, it is crucial to study the differences in seepage characteristics and make informed choices regarding suitable energy supplement modes for different reservoir types.

Numerous studies have extensively indicated that the microscopic pore-throat structure, encompassing factors such as size, number, volume, geometry, distribution, and connectivity of pores and throats, is the primary factor influencing the seepage characteristics of different reservoirs (Katz and Thompson, 1985; Krohn, 1988; Lian et al., 2004; Zeng et al., 2007; Zhao et al., 2008). Various experimental methods are employed to investigate microscopic pore-throat structures, including X-ray diffraction, casting thin sections, scanning electron microscopy, high-pressure and constant-speed mercury intrusion capillary pressure, nuclear magnetic resonance (NMR), and X-ray computed tomography (CT) scanning (Gao and Li, 2016; Chen et al., 2017; Xiao et al., 2020; Saafan et al., 2022). These methods provide insights into morphological characteristics, size distribution, spatial structure, and the formation causes of microscopic pore-throat structures. Additionally, it has been concluded through the utilization of these methods that multistage pore-throat characteristics are prevalent in hydrocarbon reservoirs (Chen et al., 2017; Yin et al., 2019; Zhu et al., 2019). The pore-throat structure is a crucial factor directly impacting two-phase flow (Ramstad et al., 2019; Ju et al., 2020; Liu et al., 2020; He et al., 2021). However, to the best of our knowledge, the impact mechanism of these multistage pore-throat structures on two-phase flows remains unclear.

Relative permeability curves are widely employed to depict the seepage characteristics of two-phase flows in various reservoir types (Honarpour and Mahmood, 1988; Alamooti et al., 2018; Liu et al., 2019, 2024; Mirzaei-Paiaman et al., 2019; Chen et al., 2022). However, previous studies have predominantly focused on the internal variations in the relative permeability curves (Liu et al., 2006; Nguyen et al., 2006; Zhang et al., 2006), the influence of external factors such as temperature and pressure (Esmaeili et al., 2019; Iyi et al., 2022), and the non-Darcy seepage in low-permeability or tight reservoirs (Li and Yang, 2008; Dou, 2013). In the study of seepage characteristics in porous media, Li and Horne established a model for spontaneous imbibition experiments that incorporates the effects of gravity and capillary pressure (Li and Horne, 2001, 2005a, b, 2006, 2007). This model exhibits a linear relationship between oil production rate and reciprocal values of oil recovery. In 2019, Wang et al. extended the model from the imbibition system to the flooding system, validating the reliability of the Li–Horne model through numerous displacement experiments and production data (Wang et al., 2019a). Hence, the use of the Li–Horne model for characterizing two-phase flow is considered reliably. Then, Wang et al. applied the Li–Horne model to the water-sensitive damage evaluation of low permeability sandy conglomerate reservoirs, and effectively evaluated the influence of injection water with different salinities on the seepage capacity of sandy conglomerate reservoirs (Wang et al., 2019b). However, the Li–Horne model still does not consider differential displacement pressure and movable oil saturation. Wang et al. further improved the Li–Horne model considering the influence of these two factors, and confirmed the reliability of the improved model through a large number of displacement experiments which include oil-displacement experiments of different sandstones, flooding systems, oil viscosities, injection water salinities, and pressure conditions (Wang et al., 2023).

One crucial objective in understanding two-phase flow is to optimize the flooding mode in hydrocarbon production. Currently, water flooding is the most commonly used method for energy supplementation, although the oil recovery from water flooding is generally not high. Gas flooding is considered a viable alternative for enhance oil recovery (EOR), as it offers advantages such as strong seepage capacity, high oil exchange ratio, efficient oil-displacement efficiency, potential for two-phase production, and improvement of crude oil quality (Guo et al., 2002, 2003). Gas flooding has been successfully implemented in various oil-producing countries, including United States, Russia, Canada, Algeria, among others, leading to oil recovery improvements ranging from 12% to 27%. Currently, there are more projects involving gas flooding after water flooding worldwide, and gas flooding is considered an effective mode for EOR in both new and mature oilfields (Guo et al., 2003; Kulkarni, 2005). In 2011, Fatemi et al. conducted experiments on cores to study the influence of water wetting and mixed wetting on water-alternating-gas flooding. They found that oil recovery from water-alternating-gas flooding was higher than that from water or gas flooding alone (Fatemi et al., 2011). Additionally, oil recovery from gas flooding was higher than that from water flooding under the same wettability conditions, and the highest oil recovery was observed with water-alternating-gas flooding. The flooding mode of early water flooding followed by immiscible CO_2 flooding or associated gas flooding was proven to be effective for EOR when compared to water flooding alone. For example, in the Daqing Oilfield, pilot production demonstrated a 6% increase in oil recovery (Guo et al., 2003). Similarly, the long-core tests were conducted in the Weiji-sangwen Oilfield, and the oil recovery was enhanced by 5%–12% (Guo et al., 2002). Furthermore, CO_2 flooding after water flooding is suitable for reservoirs with high-viscosity oil, while hydrocarbon gas and N_2 flooding after water flooding are suitable for reservoirs with low-viscosity oil (Guo et al., 2003). Therefore, after understanding the gas source and oil properties of the LSG Formation and the impact mechanisms of the multistage pore-throat structure on seepage, it is necessary to conduct further experiments on associated gas flooding after water flooding to gain insight into the flooding mode.

In this study, the main factors affecting seepage capacity and oil-displacement efficiency of different reservoirs were identified through numerous microscopic pore-throat experiments. The improved evaluation method of two-phase flow based on the Li–Horne model was used to analyze the seepage behavior of reservoirs with varying permeabilities and lithologies in the LSG Formation of the BBW Basin, and to establish the relationship between seepage behavior and microscopic pore-throat structure. Based on this analysis, the differences in seepage capacity and oil-displacement efficiency under different flooding fluids and modes were examined to determine a reasonable mode of energy supplementation for different reservoirs in the BBW Basin. This study aims to provide experimental insights into the relationship between pore structure, fluid flow, and dynamic flooding modes. The innovation lies in establishing the relationship between the microscopic pore structure of different reservoirs and the seepage behavior of two-phase fluids, bridging the gap between microscopic pore throats and macroscopic seepage, and clarifying the methods, mechanisms, and effects of enhancing oil recovery in different reservoirs.

2. Theoretical backgrounds

2.1. Fractal model of capillary pressure

The oil and gas storage and seepage spaces in porous media consist of pores and throats. The spatial distribution of pores and throats exhibits statistical self-similarity, meaning that the probability distribution of certain enlarged parts is identical to that of the larger part. This characteristic can be described using fractal geometry (Katz and Thompson, 1985; Cai et al., 2015, 2017). According to the fractal theory, the relationship between the number of pores $N(r)$ and radius r is as follows (Yu and Cheng, 2002; Li, 2010):

$$N(r) \propto r^{-D} \tag{1}$$

where $N(r)$ is the number of pores; r is the pore radius, μm; D represents the fractal dimension.

For a single cylindrical capillary with radius r and length L_c, the volume is $\pi r^2 L_c$. According to the capillary model, $N(r)$ can be expressed as follows:

$$N(r) = \frac{V_{Hg}}{\pi r^2 L_c} \tag{2}$$

where L_c represents the capillary length, μm; V_{Hg} represents the total volume of mercury intruded into the rock samples, μm³.

Combining Eqs. (1) and (2) gives

$$\frac{V_{Hg}}{\pi r^2 L_c} \propto r^{-D} \tag{3}$$

Assuming that length is a function of radius, for a three-dimensional pore space, and assuming $L_c \propto r$, then

$$V_{Hg} \propto r^{3-D} \tag{4}$$

According to the Young−Laplace equation, the capillary pressure is inversely proportional to the pore-throat radius; thus, Eq. (4) can be written as (Kate and Gokhale, 2006)

$$V_{Hg} \propto P_c^{-(3-D)} \tag{5}$$

Mercury saturation is equal to the total volume of the mercury intruded rock sample/pore volume of the rock sample.

$$S_{Hg} = \alpha P_c^{-(3-D)} \tag{6}$$

where α is a constant; P_c is the capillary pressure obtained by the mercury injection experiment, MPa; S_{Hg} is the mercury saturation. This indicates that the relationship between mercury saturation and capillary pressure in the rock sample satisfies the power law. By taking the logarithm of both sides of Eq. (6), the following can be obtained

$$\lg S_{Hg} = (D - 3)\lg P_c + C \tag{7}$$

In a logarithmic coordinate system, $\lg S_{Hg}$ and $\lg P_c$ exhibit a linear relationship, where C is a constant.

2.2. Two-phase seepage model

Assuming spontaneous imbibition takes place in a vertically positioned rock sample, the seepage velocity equations for the wetting and non-wetting phases are as follows:

$$v_w = -\frac{k_w}{\mu_w}\left(\frac{\partial p_w}{\partial x} + \rho_w g\right) \tag{8a}$$

$$v_{nw} = -\frac{k_{nw}}{\mu_{nw}}\left(\frac{\partial p_{nw}}{\partial x} + \rho_{nw} g\right) \tag{8b}$$

where v_w and v_{nw} represent the seepage velocities of the wetting and non-wetting phases, respectively, cm³/min; k_w and k_{nw} are the effective permeabilities of the wetting and non-wetting phases, respectively, mD; μ_w and μ_{nw} are the viscosities of the wetting phases and non-wetting phases, respectively, cP; ρ_w and ρ_{nw} are the densities of the wetting and non-wetting phases, respectively, g/cm³; p_w and p_{nw} are the pressures of the wetting and non-wetting phases when the distance is x, MPa; g is the gravity constant, m/s².

From the definition of capillary pressure, the pressure equation of the wetting phase can be written as

$$p_w = p_{nw} - P_c \tag{9}$$

where P_c denotes the capillary pressure. Substituting Eq. (9) into Eq. (8a) gives

$$v_w = M_w\left(\frac{\partial P_c}{\partial x} - \frac{\partial p_{nw}}{\partial x} - \rho_w g\right) \tag{10}$$

where $M_w = \frac{k_w}{\mu_w}$. Eq. (8b) can be reorganized as

$$\frac{\partial p_{nw}}{\partial x} = -\left(\frac{v_{nw}}{M_{nw}} + \rho_{nw} g\right) \tag{11}$$

where $M_{nw} = \frac{k_{nw}}{\mu_{nw}}$. In the process of reverse imbibition,

$$v_w + v_{nw} = 0 \tag{12}$$

Considering the reverse imbibition process, Eq. (11) can be simplified as

$$\frac{\partial p_{nw}}{\partial x} = \frac{v_w}{M_{nw}} - \rho_{nw} g \tag{13}$$

Substituting Eq. (13) into Eq. (10), the velocity of the wetting phase can be expressed as

$$v_w = \frac{M_{nw} M_w}{M_{nw} + M_w}\left(\frac{\partial P_c}{\partial x} - g\right) \tag{14}$$

where $\Delta\rho$ is the density difference between the wetting and non-wetting phases ($\Delta\rho = \rho_w - \rho_{nw}$). The effective fluidity is defined as

$$M_e = \frac{k_e}{\mu_e} = \frac{M_{nw} M_w}{M_{nw} + M_w} \tag{15}$$

where M_e is the effective fluidity, which represents the total fluidity of the wetted and non-wetted phases during imbibition, mD/cP; k_e and μ_e represent the effective permeability and viscosity of the two phases, respectively.

Based on the experimental results, it is assumed that water imbibes into air-saturated rocks in a piston-like manner in certain cases (Akin and Kovscek, 1999; Li and Horne, 2001). In a piston-like imbibition flow, the following equation is true:

$$\frac{\partial P_c}{\partial x} = \frac{P_c}{x} \tag{16}$$

Substituting Eqs. (15) and (16) into Eq. (14) gives

$$v_w = M_e\left(\frac{P_c}{x} - g\right) \tag{17}$$

Assuming a uniform distribution of S_{wi} in the porous medium, the total amount of imbibition in the wetting phase can be calculated as

$$N_{wt} = Ax\phi\left(S_{wf} - S_{wi}\right) \tag{18}$$

where N_{wt} is the total amount of imbibition in the wetting phase, cm^3; ϕ is the core porosity; A is the cross-section area of the core, cm^2; S_{wf} is the water saturation behind the imbibition front; S_{wi} is the initial wetting phase (water in this study) saturation in the core sample. Based on the imbibition velocity of the wetting phase, $q_w = Av_w$, Eq. (17) can be expressed as

$$q_w = AM_e\left(\frac{P_c}{x} - g\right) \tag{19}$$

In Eq. (19), P_c and M_e are the capillary pressure and effective mobility, respectively. We define $P_c = P_c(S_{wf})$ and $M_e = M_e(S_{wf})$ to distinguish capillary pressure and effective mobility from any other water saturation. After substituting Eq. (18) into Eq. (19), the following equation is obtained

$$q_w = a_0\frac{1}{R} - b_0 \tag{20}$$

with

$$a_0 = \frac{AM_e^*\left(S_{wf} - S_{wi}\right)}{L}P_c^*$$

$$b_0 = AM_e^*\Delta\rho g$$

$$M_e^* = \frac{M_w^* M_{nw}^*}{M_w^* + M_{nw}^*}$$

$$M_w^* = \frac{k_w^*}{\mu_w}$$

$$M_{nw}^* = \frac{k_{nw}^*}{\mu_{nw}}$$

$$R = \frac{N_{wt}}{V_p} = \frac{N_{wt}}{AL\phi}$$

where a_0 and b_0 are two constants associated with capillary and gravity forces, respectively; q_w is the imbibition rate of the wet phase, cm^3/min; R is the recovery in the unit of pore volume; M_e^* is the global mobility of two-phase fluids, mD/cP; M_w^* is the wetting phase mobility at S_{wf}, mD/cP; M_{nw}^* is the non-wetting phase mobility at $1 - S_{wf}$, mD/cP; P_c^* is the capillary pressure at S_{wf}, MPa; L is the length of the core sample, cm; k_w^* and k_{nw}^* are the effective permeabilities of the wetting and non-wetting phases at S_{wf} and $1 - S_{wf}$, respectively, mD; V_p is the volume of the core sample, cm^3. Eq. (20) is the Li−Horne model.

During the displacement process, the speed of the entering core water was equal to the speed of the core oil displacement, that is, $q_w = q_o$. Eq. (20) can be transformed into

$$q_o = a_0\frac{1}{R} - b_0 \tag{21}$$

where q_o is the volumetric production rate, cm^3/min.

Eq. (21) represents LiHorne model which describes the seepage characteristic of both the wetting and non-wetting phases (Li and Horne, 2001, 2005a,b, 2006, 2007). For three-phase flow involving oil, gas, and water, it can be simplified as a two-phase gas−liquid flow, with oil and water considered as a combined phase (Li and Horne, 2001, 2005a, b, 2006, 2007). However, since the Li−Horne model does not account for the effects of temperature and pressure, it may not be suitable for degassing experiments involving changes in temperature and pressure. It is recommended to maintain stable experimental temperature and pressure conditions during both imbibition and displacement experiments.

Global mobility (M_e^*) was initially used to evaluate spontaneous imbibition experiments (Nurkamelia and Arihara, 2004; Høgnesen et al., 2004; Babadagli et al., 2005; Li and Horne, 2005b; Tavassoli et al., 2005), and the effect of water flooding (Wang et al., 2019a). To eliminate the effect of displacement differential pressure on the analysis results in Eq. (21), the displacement differential pressure is divided to obtain the following equation:

$$J_o = a_1\frac{1}{R} - b_1 \tag{22}$$

with

$$J_o = q_o/\Delta p$$

$$a_1 = a_0/\Delta p$$

$$b_1 = b_0/\Delta p$$

where J_o is the oil production rate of the unit pressure differential, cm^3/(min MPa); Δp is the displacement differential pressure, MPa.

In the process of displacement, the assumptions of the two-phase seepage model include: (1) The shapes of the reservoirs are level, equal thickness, homogeneity, isotropy and isothermal. In the original state, the temperature and pressure are all original formation conditions. (2) The crude oil is not degassed in the displacement process. (3) Fluid flow in the reservoir obeys Darcy's law.

Meanwhile, an index (I_p) to evaluate the seepage capacity of water-wet sandstone reservoirs is defined as

$$I_p = \frac{M_e^*(1 - S_{wi} - S_{or})}{\Delta p} \tag{23}$$

where I_p is the new evaluation parameter of seepage capacity, mD/(cP MPa); S_{or} is the residual oil (or non-wetting phase) saturation.

The new index, I_p, incorporates various parameters related to two-phase flow, such as global mobility (M_e^*), relative storage capacity of the reservoirs ($1 - S_{wi}$), residual oil saturation (S_{or}), and displacement differential pressure (Δp). Residual oil saturation is known to be significantly influenced by factors like throat radius, reservoir heterogeneity, reserve abundance, and production mode. Therefore, the index I_p takes into account not only the permeability and relative permeability of the reservoirs but also the fluid properties, movable oil saturation ($1 - S_{wi} - S_{or}$), and displacement differential pressure (Δp). Based on this analysis, the new index provides a theoretical characterization of the seepage capacity of two-phase flow in different reservoirs.
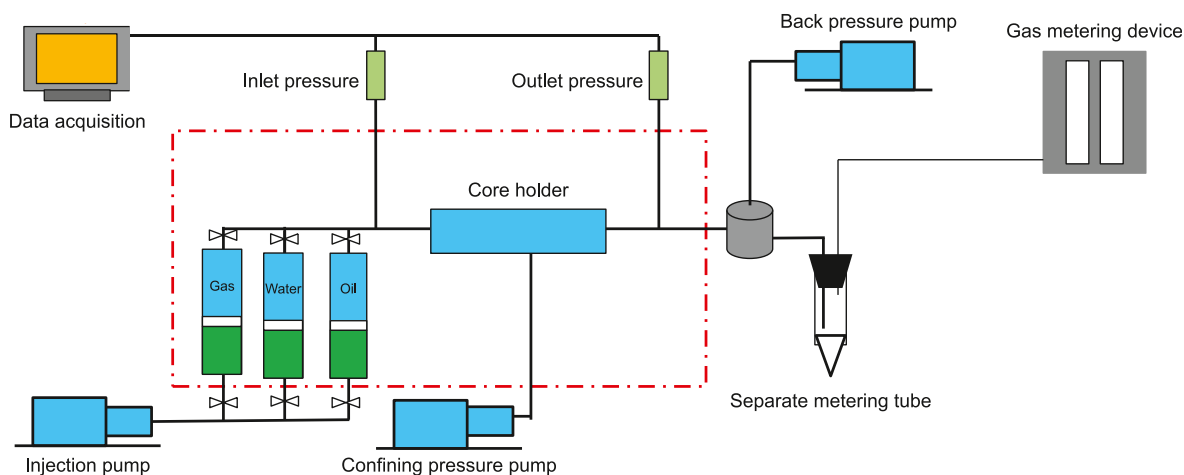
Fig. 1. Schematic diagram of the experimental apparatus used in this study for oil−water and oil−gas displacement experiments.

3. Samples and experiments

3.1. Experimental apparatus and materials

A schematic diagram of the experimental setup is presented in Fig. 1. The setup comprises several components, including a confining pressure pump, an injection pump, a back pressure pump, a core holder, a differential pressure transducer, a separate metering tube, a gas metering device, and an intermediate container. The injection pump is responsible for delivering a constant liquid injection rate or pressure to facilitate the flow of liquid through the core sample. Two types of core holders were utilized: conventional core holder and whole-diameter core holder. The conventional core holder accommodates core samples with a diameter of 2.54 cm and a length ranging from 2 to 100 cm, whereas the whole-diameter core holder can handle core samples with a diameter of 10.5 cm and a length ranging from 10 to 80 cm.

To ensure the stability of the displacement experimental apparatus, the pressure range was set between 0 and 100 MPa, while the temperature range spanned from 24 °C (room temperature) to 200 °C. For the specific displacement experiments described in this paper, the temperature range was 117.8−151.2 °C, the confining pressure range was 32.0−45.0 MPa, and the internal pressure range was 22.0−35.0 MPa (Table 1). These temperature and pressure conditions fall within the required range to maintain the stability of the experimental apparatus. All displacement experiments were conducted under the temperature and pressure conditions representative of the formation.

3.2. Core-fluid parameters and experimental conditions

Nos. 1−4 are short cores, tested with water flooding. No. 5 is a combined long core, tested with gas flooding after water flooding. No. 6 is a combined long core, tested with gas flooding and gas flooding after water flooding. Nos. 7−9 are combined long cores, tested with gas and water flooding. Lastly, No. 10, featuring a whole-diameter core, was tested with gas flooding after water flooding. The core parameters, fluid properties, and test conditions are provided in Table 1. In the case of samples with multiple core combinations, the sequence of standard cores in the combination aligns with the sample ID numbers specified in Tables 2 and 3. Notably, Nos. 2 and 6 are parallel samples, and Nos. 3, 4, 8, and 10 are also parallel samples.

The core treatment procedures and brine properties are elaborated in a previous study (Wang et al., 2019a). The gas used for injection was manually configured based on the analysis of associated gas components. The injected gas components consisted of 76.89% C_1, 10.70% C_2, 6.85% C_3, 0.81% i-C_4, 1.15% n-C_4, 3.53% CO_2, and 0.06% N_2. Under the experimental conditions, the density of the injected gas ranged from 0.20 to 0.21 g/cm^3, and the viscosity ranged from 0.024 to 0.026 cP.

4. Results and discussion

4.1. Pore-throat characteristics of different sandstones

The reservoirs in the LSG Formation of the BBW Basin consist of detrital rock with terrigenous deposits. Based on the differences in grain size, these reservoirs can be categorized into conglomeratic sandstone and conventional sandstone. The conglomeratic sandstone is further subdivided into sandy conglomerate, conglomeratic coarse sandstone, conglomeratic medium sandstone, and conglomeratic fine sandstone, while conventional sandstone is subdivided into coarse sandstone, medium sandstone, fine sandstone, and siltstone. To examine the variations in pore-throat characteristics associated with different grain sizes, we conducted analyses using methods such as casting thin sections, high-pressure and constant-speed mercury intrusion capillary pressure tests, and NMR measurements.

4.1.1. Pore characteristics

The experimental results of casting thin sections for typical detrital reservoirs with different grain sizes in the LSG Formation are presented in Fig. 2. Based on the image analysis of pore characteristics from the casting thin-section experiments, the sandy conglomerate shown in Fig. 2(a) has a burial depth of 2774.1 m, with 248 pores and an average pore size of 229.12 μm. In Fig. 2(b), the conglomeratic coarse sandstone is buried at a depth of 2618.5 m, with 307 pores and an average pore size of 175.59 μm. The coarse sandstone shown in Fig. 2(c) has a burial depth of 2462.8 m, with 359 pores and an average pore size of 150.06 μm. In Fig. 2(d), the middle sandstone is buried at a depth of 2442.80 m, with 495 pores and an average pore size of 133.12 μm. The fine sandstone shown in Fig. 2(e) is buried at a depth of 2558.0 m, with 1239 pores and an average pore size of 58.93 μm. Lastly, in Fig. 2(f), the siltstone has a burial depth of 2589.0 m, with 2584 pores and an average pore size of 34.61 μm. Thus, as the reservoir grain size decreases, the pore size also decreases while the number of pores increases. Furthermore, the conglomeratic sandstone samples exhibit larger and fewer pores compared to the conventional sandstone samples.

Table 1
Core size and petrophysical parameters, fluid properties, and test conditions.

Core No.	Lithology	Core length L, cm	Core diameter D, cm	Porosity ϕ, %	Gas permeability k_g, mD	Displacement type	Oil viscosity μ_o, cP	Water viscosity μ_w, cP	Gas viscosity μ_g, cP	Injection volume, PV	Experimental temperature, °C	Confining pressure, MPa	Internal pressure, MPa
1	Fine sandstone	7.14	2.496	19.9	22.73	Water flooding	1.89	1.11		47.30	151.2	45.0	35.0
2	Conglomeratic sandstone	4.81	2.493	18.4	45.60	Water flooding	0.81	1.09		48.50	146.5	42.0	32.0
3	Conglomeratic sandstone	5.30	2.455	19.1	26.90	Water flooding	3.95	1.08		26.80	117.8	34.6	24.6
4	Conglomeratic sandstone	2.71	2.476	17.8	12.09	Water flooding	3.95	1.08		47.20	117.8	34.6	24.6
5	Fine sandstone	54.86	2.505	22.7	102.00	Gas flooding after water flooding	0.80	1.02	0.024	28.73/2.02	114.0	32.0	22.0
6	Conglomeratic sandstone	57.80	2.514	19.5	59.00	Gas flooding Gas flooding after water flooding	0.81 0.81	1.09	0.026 0.026	2.45 30.65/1.50	146.5	42.0	32.0
7	Fine sandstone	63.04	2.511	15.6	35.90	Gas flooding Water flooding	0.75 0.75	1.03	0.025	5.01 30.39	120.0	40.0	30.0
8	Conglomeratic sandstone	80.76	2.481	21.3	10.88	Gas flooding Water flooding	3.95 3.95	1.08	0.024	1.45 32.00	117.8	34.6	24.6
9	Fine sandstone	61.75	2.506	12.6	2.62	Gas flooding Water flooding	1.34 1.34	1.03	0.025	3.05 29.03	127.4	38.5	28.5
10	Conglomeratic sandstone	20.05	10.145	18.4	77.05	Gas flooding after water flooding	3.95	1.08	0.024	0.96/1.10	117.8	34.6	24.6

The microscopic pore-throat structures of the core samples were initially analyzed on a single plane in the casting thin-section experiments. Subsequently, further investigation was conducted using mercury intrusion experiments to study the samples as a whole. Fig. 3 illustrates the relationship between $\lg S_{Hg}$ and $\lg P_c$ in the mercury intrusion process and the distribution of pore radii for core samples with different lithologies and permeabilities from the LSG Formation. The fitting of $\lg S_{Hg}$ and $\lg P_c$ based on Eq. (7) is also depicted in Fig. 3. The following observations can be made: (1) For fine sandstone samples with a gas-based permeability exceeding 50 mD, the plots of $\lg S_{Hg}$ vs. $\lg P_c$ exhibit two-stage characteristics. Stage I corresponds to low mercury intrusion pressure with a steep slope, indicating the fractal characteristics of large pores. Stage II represents the fractal characteristics of small pores, and the turning point of the two-stage fitting curves aligns with the peak pore radius (Fig. 3(a)). (2) In contrast, fine sandstone samples with a gas-based permeability below 50 mD display a three-stage fitting feature. The plot of $\lg S_{Hg}$ vs. $\lg P_c$ indicates the presence of only a few large pores (Stage I). The turning points of the fitting curve for Stages II and III correspond to the peak pore radius (Fig. 3(b)). (3) Conglomeratic sandstone samples with a gas-based permeability exceeding 50 mD exhibit a three-stage fitting feature. The turning points of the fitting curve for Stages I, II, and III align with the two peak radii of the pores (Fig. 3(c)). (4) Conglomeratic sandstone samples with a gas-based permeability below 50 mD demonstrate a four-stage fitting feature. Similar to the higher-permeability conglomeratic sandstone, Stage I represents the presence of a few large pores. The turning points of the fitting curve for Stages II, III, and IV correspond to the two peak radii of the pores (Fig. 3(d)). Based on the above analysis, under the same lithologic conditions, low-permeability sandstone exhibits a smaller number of large pores compared to medium- and high-permeability sandstones, resulting in an additional stage of pore fractal characteristics. Additionally, conglomeratic sandstone displays longer pore fractal characteristics than fine sandstone due to its strong heterogeneity, leading to bimodal pore characteristics observed in the experiments. Moreover, the pore distribution range of conglomeratic sandstone is broader, with a larger proportion of macropores (Fig. 3).

To investigate the variation in pore size ratios among different lithology reservoirs, a large number of water-saturated core samples were subjected to NMR testing. The NMR measurements were conducted using the RecCore-2515 NMR Detection System of On-line Saturation. Based on previous studies (Liu et al., 2009; Zhang et al., 2018) and established criteria in BBW Basin (Wang et al., 2019b; Jiang et al., 2021), the microscopic pores were categorized into macropores, mesopores, and micropores during the NMR experiments. Specifically, macropores were characterized by T_2 values (transverse relaxation time) greater than 86.40 ms, mesopores exhibited T_2 values ranging from 11.57 to 86.40 ms, and micropores possessed T_2 values less than 11.57 ms. Micropores were associated with immovable oil, whereas macropores and mesopores were attributed to movable oil.

Fig. 4 illustrates the relationship between gas permeability and the volume proportion of different pore sizes for distinct lithologies, specifically conglomeratic sandstone (25 core samples) and fine sandstone (34 core samples) within the LSG Formation. The cores used in the study were representative samples from blocks within the BBW Basin. As depicted in Fig. 4, the volume proportion of macropores and mesopores increased with higher gas permeability, while the proportion of micropores decreased. Consequently, macropores and mesopores were identified as the primary factors influencing gas permeability. In general, the volume proportion of macropores was higher in conglomeratic sandstone samples compared to fine sandstone samples (Fig. 4(a)), whereas

Table 2
Core size and petrophysical parameters of the samples with multiple core combinations (Nos. 5–7).

Core No.	D, cm	L, cm	ϕ, %	k_g, mD	Core No.	D, cm	L, cm	ϕ, %	k_g, mD	Core No.	D, cm	L, cm	ϕ, %	k_g, mD
5–1	2.502	4.83	22.5	103.00	6–1	2.507	5.00	19.5	41.00	7–1	2.519	7.35	15.4	25.60
5–2	2.518	4.39	21.8	93.00	6–2	2.506	4.99	19.6	48.40	7–2	2.520	7.19	15.9	36.00
5–3	2.513	4.96	20.4	115.00	6–3	2.519	2.72	19.0	26.00	7–3	2.517	6.14	15.1	36.90
5–4	2.504	4.13	22.9	82.90	6–4	2.509	4.65	18.8	26.20	7–4	2.502	6.82	16.1	37.80
5–5	2.502	4.70	22.5	122.00	6–5	2.507	5.00	19.7	59.00	7–5	2.510	7.49	14.9	17.60
5–6	2.502	4.82	20.1	149.00	6–6	2.511	5.19	18.6	24.50	7–6	2.502	7.36	16.2	40.60
5–7	2.504	4.41	24.4	158.00	6–7	2.537	5.35	20.2	73.40	7–7	2.509	6.78	14.8	15.80
5–8	2.505	4.42	21.4	27.90	6–8	2.511	5.11	17.7	13.00	7–8	2.511	7.20	16.1	54.50
5–9	2.500	4.10	24.9	198.00	6–9	2.509	4.99	20.3	92.50	7–9	2.508	6.71	15.4	58.40
5–10	2.506	4.79	23.3	181.00	6–10	2.505	5.12	20.5	102.10					
5–11	2.502	5.55	24.5	215.00	6–11	2.509	5.10	20.3	76.30					
5–12	2.502	3.76	23.9	169.00	6–12	2.539	4.58	19.1	124.10					
Overall parameter		54.86	22.7	102.00	Overall parameter		57.80	19.5	59.00	Overall parameter		63.04	15.6	35.90

Table 3
Core size and petrophysical parameters of the samples with multiple core combinations (Nos. 8–9).

Core No.	D, cm	L, cm	ϕ, %	k_g, mD	Core No.	D, cm	L, cm	ϕ, %	k_g, mD
8–1	2.473	5.38	19.9	10.66	9–1	2.508	5.25	13.8	2.28
8–2	2.461	4.79	20.7	10.43	9–2	2.513	5.74	12.2	2.08
8–3	2.481	4.78	18.1	10.42	9–3	2.506	5.17	11.8	3.36
8–4	2.481	5.56	19.6	11.50	9–4	2.504	5.94	11.3	1.59
8–5	2.481	5.30	21.5	11.94	9–5	2.505	6.34	12.1	3.97
8–6	2.481	6.51	25.1	9.70	9–6	2.507	4.90	11.5	1.57
8–7	2.481	5.37	20.4	13.31	9–7	2.505	5.60	11.6	4.35
8–8	2.481	5.82	19.2	8.40	9–8	2.511	6.80	14.2	4.39
8–9	2.481	5.65	26.8	14.17	9–9	2.515	5.62	12.9	1.47
8–10	2.481	5.85	20.2	8.36	9–10	2.509	4.80	14.7	4.66
8–11	2.481	5.24	23.2	16.22	9–11	2.508	5.59	14.4	6.83
8–12	2.473	5.38	19.9	10.66					
8–13	2.461	4.79	20.7	10.43					
8–14	2.481	4.78	18.1	10.42					
8–15	2.481	5.56	19.6	16.22					
Overall parameter		80.76	21.3	10.88	Overall parameter		61.75	12.6	2.62
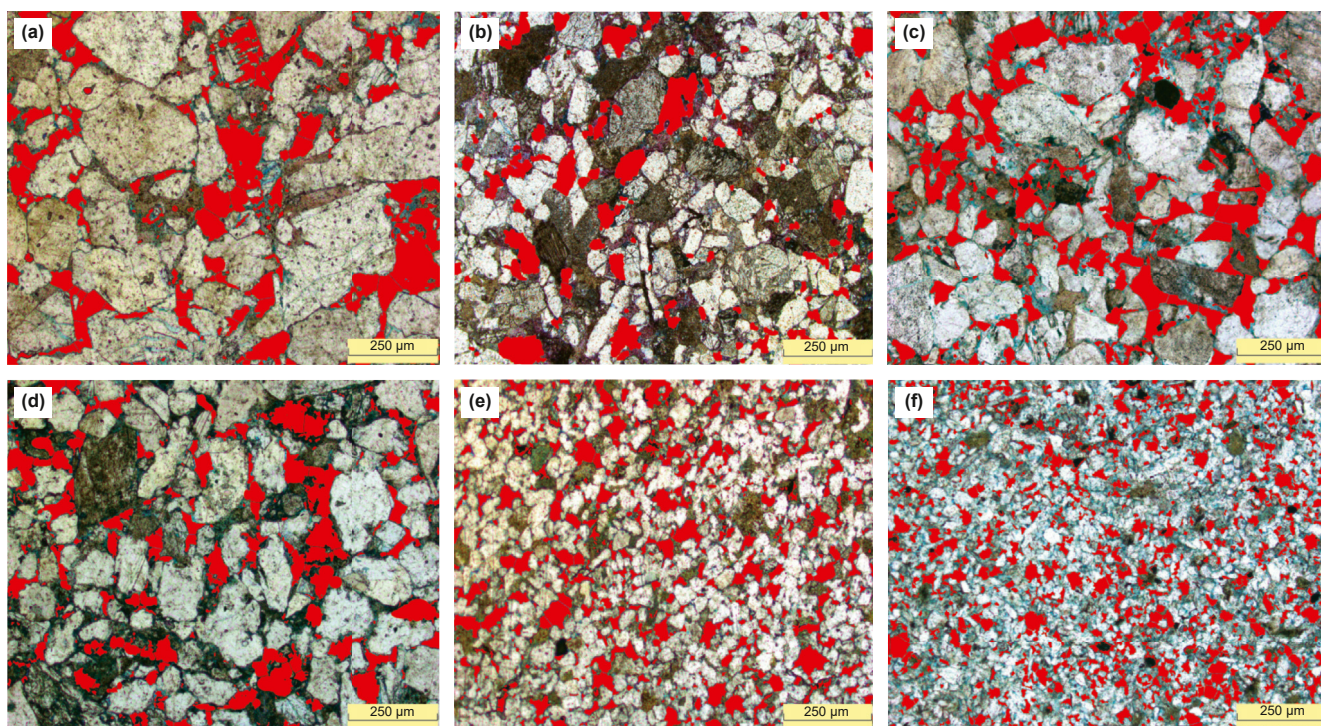
Fig. 2. Experimental results of casting thin sections for various sandstone samples selected from representative blocks in the LSG Formation of the BBW Basin. The thin sections include samples of sandy conglomerate (**a**), conglomeratic coarse sandstone (**b**), coarse sandstone (**c**), medium sandstone (**d**), fine sandstone (**e**), and siltstone (**f**).
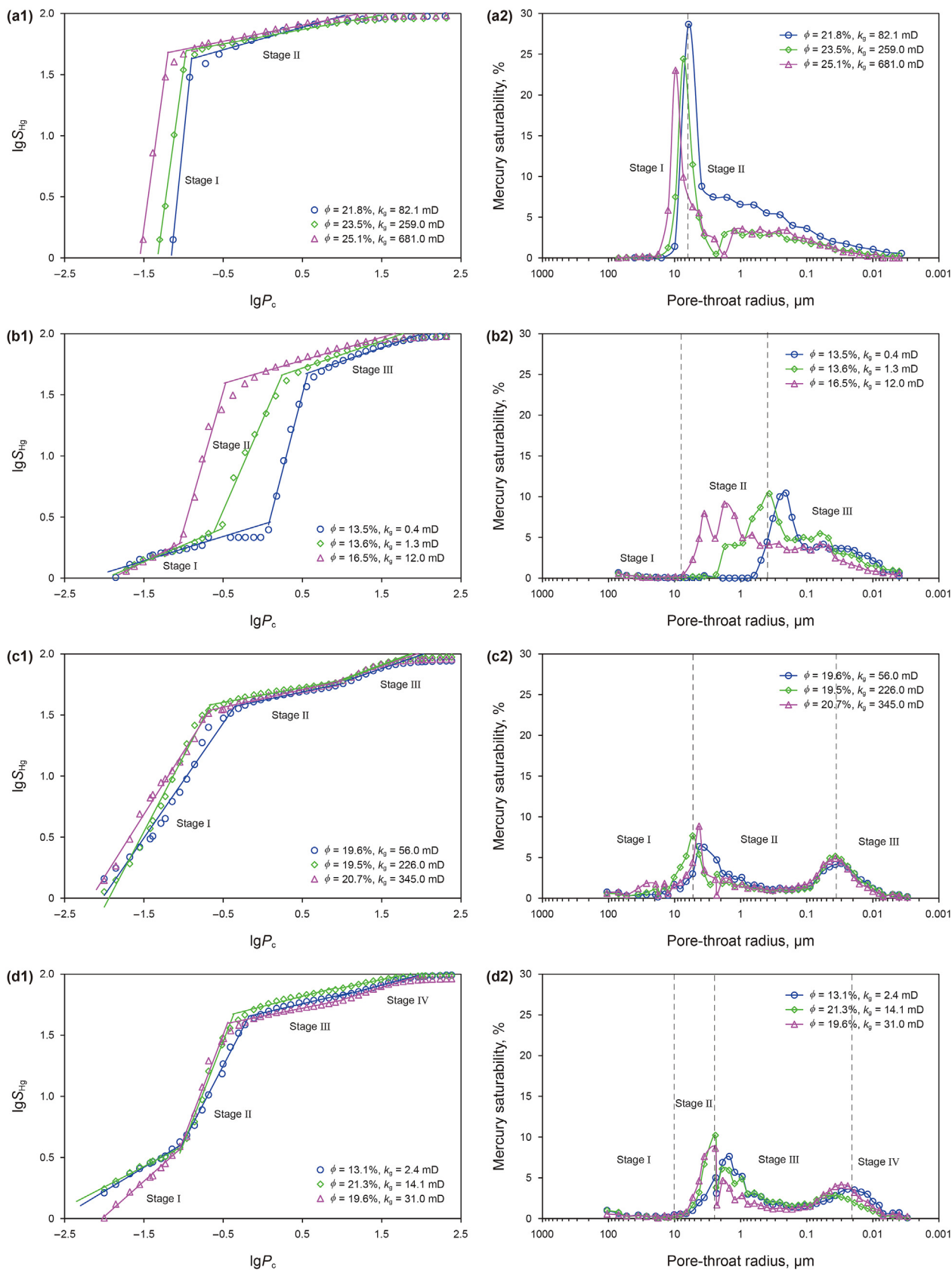
Fig. 3. Relationships between lgS_{Hg} and lgP_c in the mercury intrusion process for fine sandstone samples with a gas-based permeability of more than 50 mD (**a1**) and less than 50 mD (**b1**) and for conglomeratic sandstone samples with a gas-based permeability o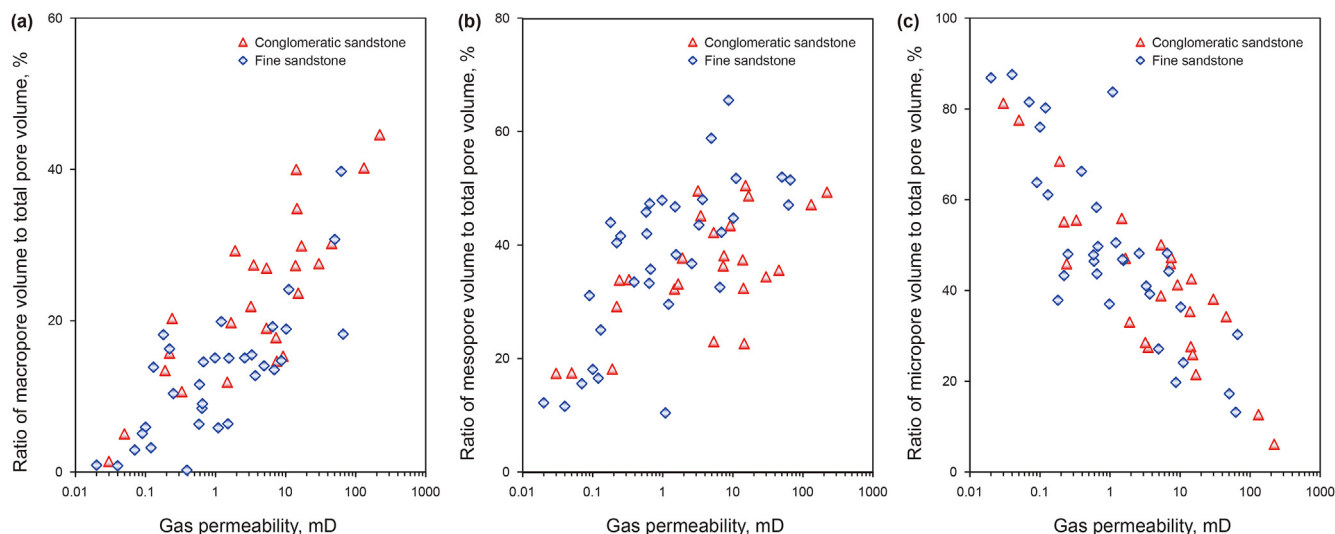f more than 50 mD (**c1**) and less than 50 mD (**d1**). Distribution of pore-throat radii for fine sandstone samples of more than 50 mD (**a2**) and less than 50 mD (**b2**) and for conglomeratic sandstone samples with a gas-based permeability of more than 50 mD (**c2**) and less than 50 mD (**d2**).

Fig. 4. Relationships between gas permeability and the volume proportion of macropores (**a**), mesopores (**b**), and micropores (**c**) from the NMR results.

the proportion of mesopores was smaller in conglomeratic sandstone samples compared to fine sandstone samples (Fig. 4(b)).

4.1.2. Throat characteristics

Pang et al. proposed that the number of effective throats per unit pore volume and throat size are the primary factors influencing reservoir permeability (Pang et al., 2017). According to their findings, the maximum throat radius, main throat radius, and effective throat volume per unit pore volume exhibit successive increases in their impact on permeability. Therefore, the size, quantity, and volume of throats in different sandstones play a crucial role in determining their seepage capacity. The pore-throat parameters were determined through constant-speed mercury intrusion experiments conducted using the ASPE730 Constant-speed Mercury Intrusion Instrument. Fig. 5 presents the characteristics of effective throats with different sandstones, including their sizes, number/volume per unit pore volume, and distribution. These data were obtained from six core samples of conglomeratic sandstone, four core samples of medium sandstone, and 19 core samples of fine sandstone from the LSG Formation. The cores used in the study were representative samples collected from blocks within the BBW Basin. The figures illustrate that the main and maximum throat radii of conglomeratic sandstone samples are larger than those of conventional sandstone samples with similar gas permeability (Fig. 5(a) and (b)). However, the number and volume of effective throats per unit pore volume in conglomeratic sandstone samples were smaller compared to the medium/fine sandstone samples (Fig. 5(c) and (d)). This disparity is a critical factor influencing the seepage behavior of the reservoir.

In summary, according to the above analysis, conglomeratic sandstone exhibits larger pores and throats, a higher proportion of macropores, a smaller number and volume of effective throats per unit pore volume, wider distribution and stronger discontinuity of the pores and throats, as well as stronger heterogeneity compared to conventional sandstone. The subsequent section will focus on investigating how these differences in pore-throat characteristics influence the seepage effect, behavior, and capacity.

4.2. Seepage characteristics

4.2.1. Microscopic displacement effect difference

As mentioned earlier, the comparative analysis of pore-throat distribution for reservoirs with different granularities indicates that conglomeratic sandstone exhibits stronger reservoir heterogeneity compared to conventional sandstone. To investigate the influence of reservoir heterogeneity on the displacement effect, microscopic visualization displacement experiments were conducted. The experimental setup included a microscope (Nikon SMZ1270), a computer, a core-slice holder, a micro-displacement pump, a thermostatic control system, and data acquisition software. The reflection micro magnification test method was employed to observe the microscopic distribution of water flooding. The dynamic images of the water flooding process were automatically collected by the computer. Simulated oil and displacement water, containing dyes, were used in the microscopic visualization displacement experiments. The simulated oil, dyed with oil-soluble red, was made of clean oil to ensure the correct viscosity. The displacement water was dyed with methyl blue. The initially saturated water contained undyed formation water. Core slices, measuring 1 cm × 1 cm × 0.3 cm, were obtained from various cores in the LSG Formation.

The experimental process consisted of the following steps: (1) cutting the core into slices and observing them using a metallographic microscope at different magnifications; (2) vacuuming and saturating the observed core slice, placing it in the holder, and connecting the pipeline; (3) applying confining pressure to the holder and saturating the core slice with formation water to establish the initial water saturation; (4) using simulated oil to displace the formation water and recording the image until no further changes occurred, establishing the bound water saturation; (5) displacing the simulated oil with methyl blue-dyed water and recording the image until it remained unchanged for an extended period; (6) using a micro-displacement pump to inject dyed formation water into the core slice saturated with simulated oil, continuously photographing the camera area of the core slice, and observing and recording the dynamic process of the images until no further changes occurred; (7) utilizing image recognition software to process the images before and after displacement and comparing and analyzing the differences in oil and water distribution. Figs. 6 and 7 present the comparative results of microscopic visualization before and after water flooding for fine sandstone and sandy conglomerate, respectively. The water flooding parameters for the fine sandstone sample were as follows: porosity of 17.9%, gas permeability of 44.6 mD, pore volume injection rate of 206
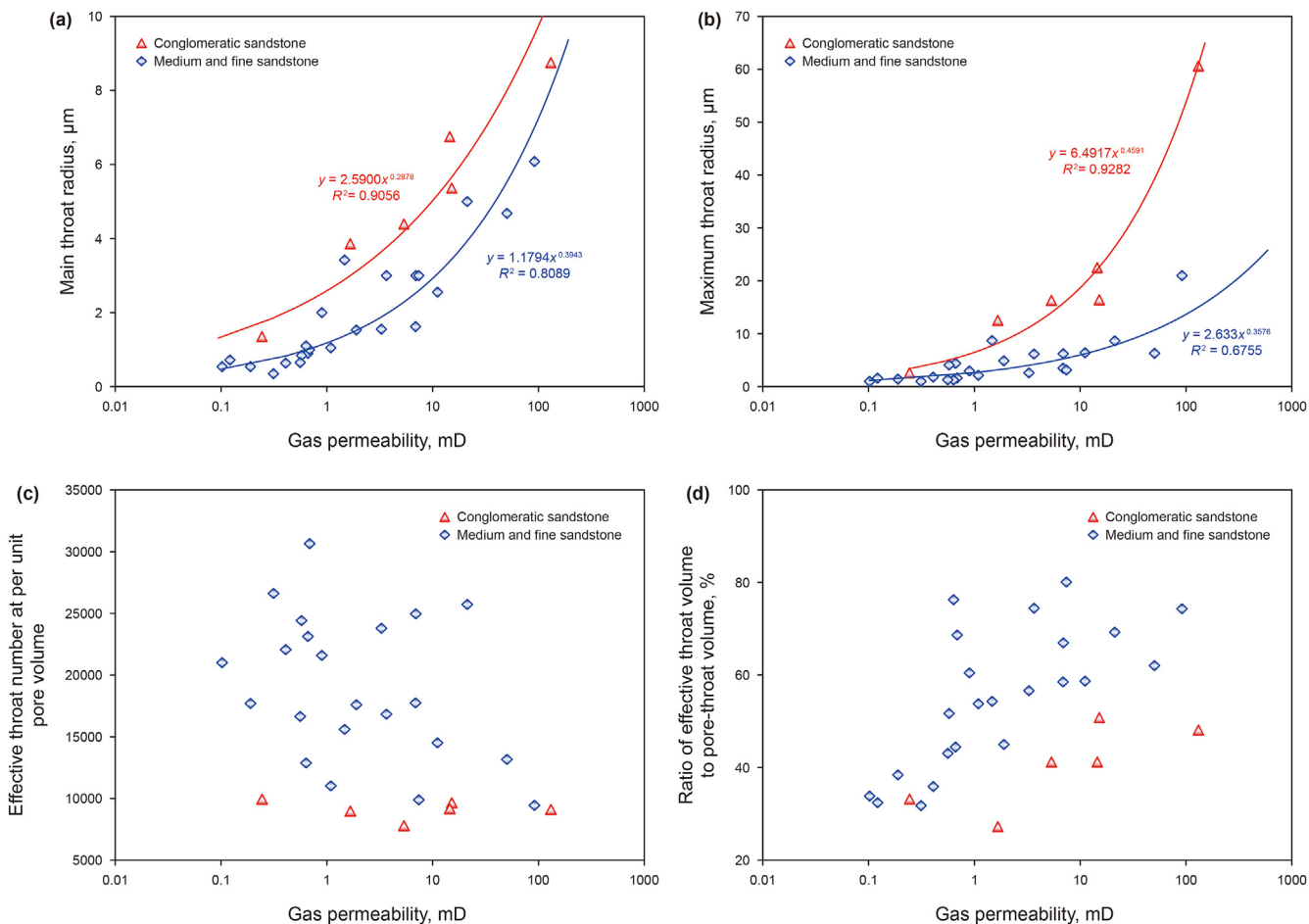
Fig. 5. Relationships between the main throat radius (**a**), maximum throat radius (**b**), effective throat number at per unit pore volume (**c**), ratio of effective throat volume to pore-throat volume (**d**) and gas permeability in different samples.
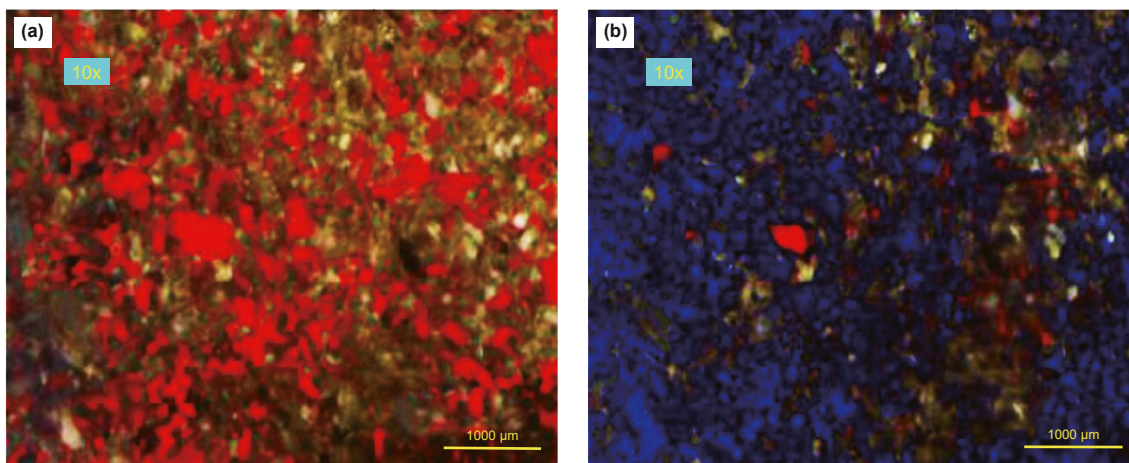

Fig. 6. Microscopic visualization results before (**a**) and after (**b**) water flooding of the fine sandstone sample.

(displacement fluid volume/pore volume), oil displacement efficiency of 88.3%, and residual oil saturation of 5.7%. Meanwhile, the water flooding parameters of the sandy conglomerate sample were as follows: porosity of 13.4%, gas-based permeability of 49.1 mD, pore volume injection rate of 301 (displacement fluid volume/pore volume), oil displacement efficiency of 41.5%, and residual oil

saturation of 61.1%. Consequently, the displacement effect of the fine sandstone sample is significantly superior to that of the sandy conglomerate sample. This disparity can be differences in pore-throat size, number, and distribution, resulting in stronger heterogeneity and lower oil displacement efficiency in the sandy conglomerate sample.
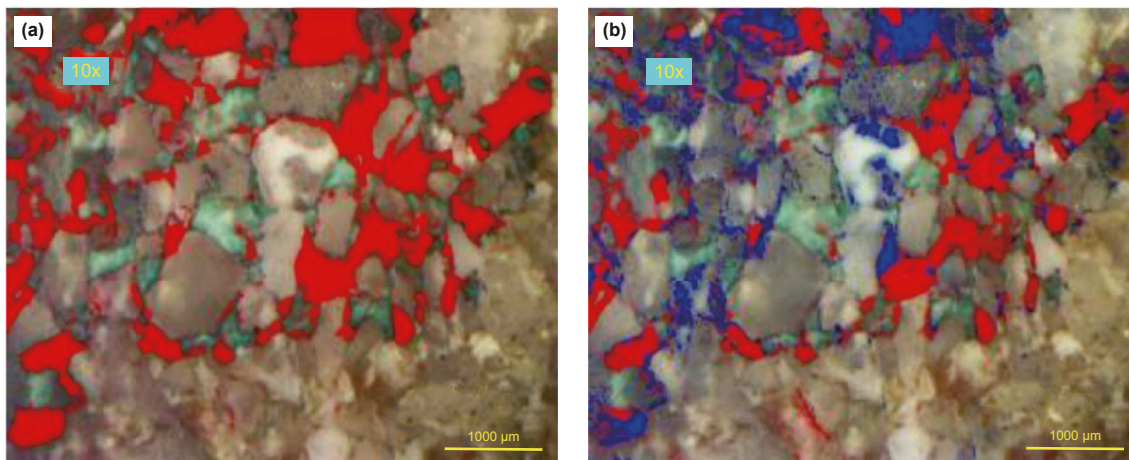
Fig. 7. Microscopic visualization results before (**a**) and after (**b**) water flooding of the sandy conglomerate sample.

4.2.2. Differences in seepage behavior

The fitting results of the water flooding process and the corresponding relationships between $\lg S_{Hg}$ and $\lg P_c$ in the mercury intrusion process for sample Nos. 5, 7, 6, and 3 are depicted in Fig. 8. It is evident that the segmented characteristics of the water flooding curves, considering different lithologies and physical properties, align well with the segmented characteristics of the mercury intrusion curves of parallel samples. This consistent matching relationship is in line with the findings presented in Fig. 3. The anhydrous oil recovery period of fine sandstone sample No. 5, which has a gas-based permeability of more than 50 mD, corresponds to Stage I in the water flooding process. For fine sandstone sample No. 7, with a gas-based permeability of less than 50 mD, the anhydrous oil recovery period corresponds to Stages I and II in the water flooding process. Regarding conglomeratic sandstone samples No. 6, with a gas-based permeability of more than 50 mD, and No. 3, with a gas-based permeability of less than 50 mD, the anhydrous oil recovery period in the water flooding process corresponds to Stage I. In the oil−water production stage, fine sandstone exhibits a single law of diminishing, whereas conglomeratic sandstone demonstrates two- or three-section laws of diminishing. Consequently, the seepage laws observed in different reservoirs are controlled by the distribution of pore-throat sizes. The seepage behavior of conglomeratic sandstone is strongly influenced by its significant heterogeneity, resulting in more complex seepage characteristics compared to fine sandstone. Particularly in the oil−water production stage, conglomeratic sandstone exhibits multiple stages of seepage characteristics.

The fitting results of the gas flooding process for sample Nos. 7 and 6 are illustrated in Fig. 9. The seepage characteristics observed during gas flooding align with those of water flooding and pore-throat distribution. Specifically, the seepage characteristics of sample No. 7 during gas flooding can be divided into three stages as shown in Fig. 9(a). Similarly, the seepage characteristics of sample No. 7 during water flooding are also divided into three stages, as depicted in Fig. 8(b1), while the pore-throat distribution characteristics of the parallel sample of No. 7 exhibit three stages in Fig. 8(b2). Similarly, the seepage characteristics of sample No. 6 during gas flooding are divided into three stages in Fig. 9(b), while the seepage characteristics of sample No. 6 during water flooding are divided into three stages in Fig. 8(c1). Furthermore, the pore-throat distribution characteristics of the parallel sample of No. 6 also exhibit three stages in Fig. 8(c2). It is worth noting that the shape of Stage I during gas flooding differs from that during water

flooding. The J_o of Stage I during gas flooding increases, whereas the J_o of Stage I during water flooding decreases. Additionally, the J_o values of gas flooding and water flooding under the original state show little difference, indicating that gas flooding requires a certain amount of time for miscibility. As the degree of miscibility increases, the productivity of gas flooding also increases. The maximum J_o value during gas flooding is 5−6 times higher than that during water flooding.

The fitting results of the water flooding process and the associated gas flooding after water flooding process for sample Nos. 5 and 6 are presented in Fig. 10. As depicted in the figure, it is evident that associated gas flooding after water flooding can effectively enhance the displacement of residual oil compared to water flooding alone in different reservoirs. The J_o of associated gas flooding after water flooding is notably higher than that of water flooding, indicating a significant improvement in reservoir productivity and oil recovery.

4.2.3. Multistage seepage capacity difference for conglomeratic sandstone

Based on the two-phase seepage model, a clear linear relationship exists between the oil productivity per unit differential pressure (J_o) and the reciprocal value of oil recovery ($1/R$), as shown in Eq. (22) and Fig. 8. Subsequently, the values of $M_e^*/\Delta p$ were calculated using $b_0 = AM_e^*\Delta\rho g$ and $b_1 = b_0/\Delta p$, as determined by Eq. (23). The evaluation results of the conglomeratic sandstone with water and gas flooding are presented in Table 4. Sample Nos. 2 and 6 are parallel samples, while sample Nos. 3 and 4 also form a parallel pair.

The seepage capacities of the stages following water breakthrough for the conglomeratic sandstone samples exhibited significantly different. Notably, larger pore throats (Stage II) played a crucial role in seepage capacity and oil displacement efficiency after water breakthrough, as indicated in Table 4. Furthermore, the seepage capacity of gas flooding was considerably greater than that of water flooding at the same stage for sample No. 6. The differences in seepage capacity and oil displacement efficiency between the two stages of gas flooding were smaller than those observed with water flooding. The oil displacement efficiency of water flooding was found to be approximately 12.9% lower than that of gas flooding. Notably, the increase in oil displacement efficiency primarily occurred after gas breakthrough in Stages II and III. Specifically, the oil displacement efficiencies of water and gas flooding in Stage II were 4.9% and 9.5%, respectively, while those in Stage III
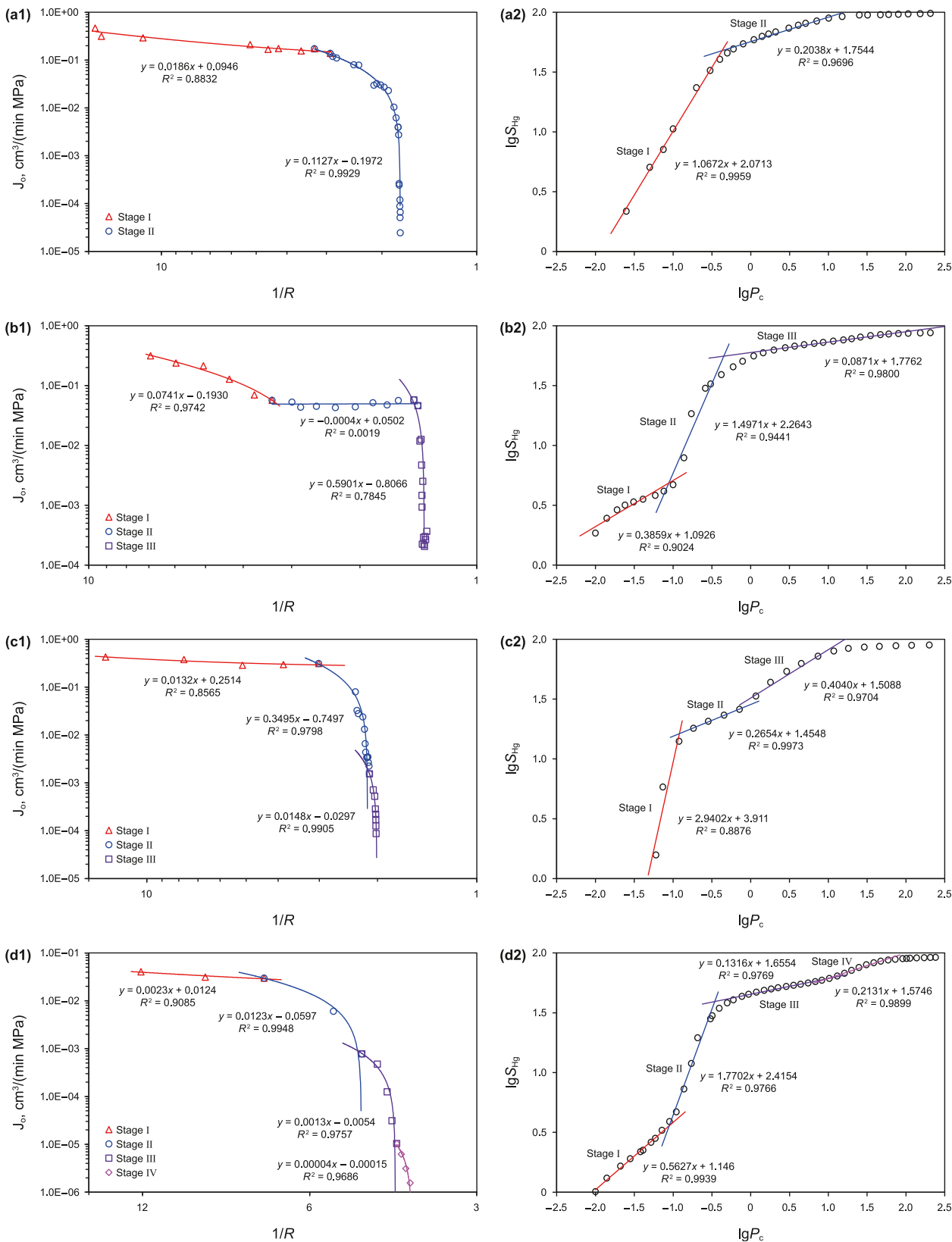
Fig. 8. Fitting results of the water flooding process of samples of No. 5 (fine sandstone) with $\phi = 22.7\%$ and $k_g = 102.0$ mD (**a1**), No. 7 (fine sandstone) with $\phi = 15.6\%$ and $k_g = 35.9$ mD (**b1**), No. 6 (conglomeratic sandstone) with $\phi = 19.5\%$ and $k_g = 59.0$ mD (**c1**), and No. 3 (conglomeratic sandstone) with $\phi = 19.1\%$, and $k_g = 26.9$ mD (**d1**). The relationships between $\lg S_{Hg}$ and $\lg P_c$ in the mercury injection process for parallel samples of No. 5 with $\phi = 21.9\%$ and $k_g = 77.0$ mD (**a2**), No. 7 with $\phi = 15.7\%$ and $k_g = 25.0$ mD (**b2**), No. 6 with $\phi = 20.4\%$ and $k_g = 71.8$ mD (**c2**), and No. 3 with $\phi = 19.6\%$ and $k_g = 31.0$ mD (**d2**).
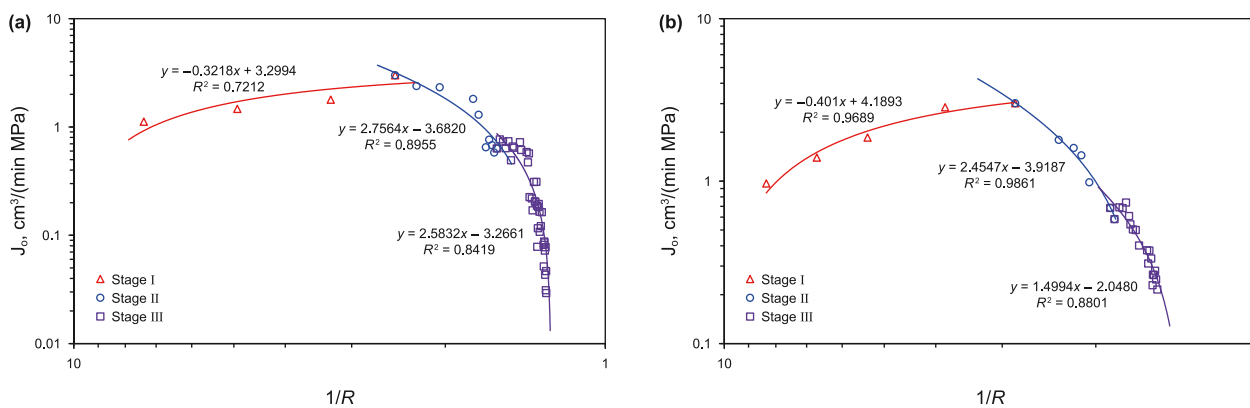
Fig. 9. Fitting results of the gas flooding process of No. 7 (fine sandstone) with $\phi = 15.6\%$ and $k_g = 35.9$ mD (**a**) and No. 6 (conglomeratic sandstone) with $\phi = 19.5\%$ and $k_g = 59.0$ mD (**b**).
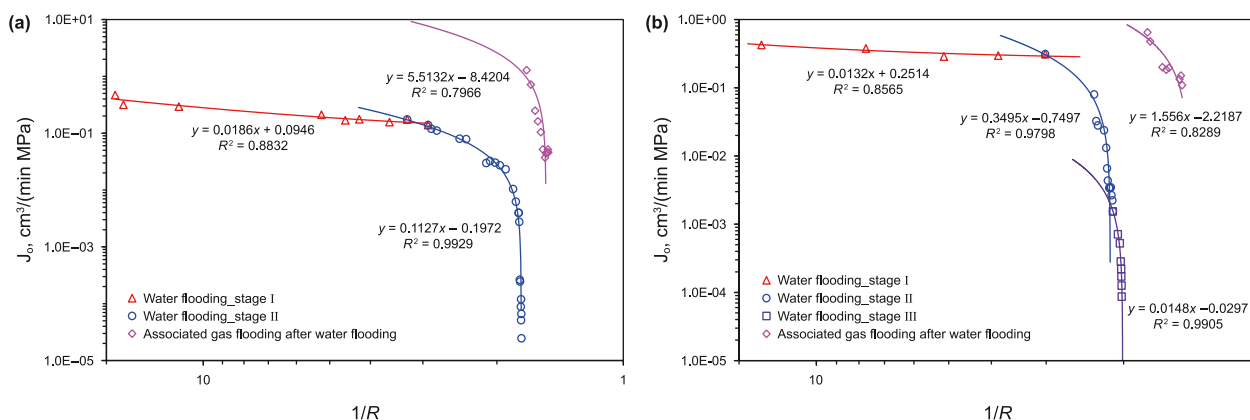

Fig. 10. Fitting results of the water flooding and associated gas flooding after water flooding process of No. 5 (fine sandstone) with $\phi = 22.7\%$ and $k_g = 102.0$ mD (**a**) and No. 6 (conglomeratic sandstone) with $\phi = 19.5\%$ and $k_g = 59.0$ mD (**b**).

Table 4
Evaluation results of the conglomeratic sandstone samples with water and gas flooding.

Core No.	Displacement type	Fitting object	I_p, mD/(cP MPa)	Oil displacement efficiency, %	Proportion of oil displacement efficiency, %
2	Water flooding	Stage II	1047.26	17.2	36.4
		Stage III	399.22	9.3	19.7
3	Water flooding	Stage II	121.50	6.9	27.3
		Stage III	8.93	3.2	12.7
		Stage VI	0.26	1.4	5.5
4	Water flooding	Stage II	49.26	15.5	38.7
		Stage III	8.56	3.6	9.1
		Stage VI	0.35	2.7	6.8
6	Water flooding	Stage II	274.47	4.9	9.9
		Stage III	10.87	2.2	4.5
	Gas flooding	Stage II	1028.38	9.5	15.3
		Stage III	509.66	16.7	26.8

were 2.2% and 16.7%, respectively. These results indicate that gas can enter the small pore-throat space (Stages II and III) due to the small size of gas molecules, suggesting significant potential for improving oil displacement efficiency.

4.3. Optimization of the energy supplement mode

To achieve better development results, displacement experiments were conducted on core samples with different lithologies and flooding systems. These experiments aim to provide guidance for optimizing the energy supplement mode.

4.3.1. Displacement characteristics of different reservoirs and fluids

The displacement results of reservoirs with different lithologies and flooding systems are depicted in Figs. 11 and 12. In Figs. 11(a) and 12(a), the oil displacement efficiencies of the fine sandstone samples were higher than those of the conglomeratic sandstone samples, and the oil displacement efficiency of gas flooding was either higher or similar to that of water flooding for the same samples. In Fig. 11(b), sample Nos. 6 and 8 exhibited early water breakthrough, rapid water cut rise, and narrow two-phase production, while sample No. 5 showed early water breakthrough, a slow rise in water cut, and broad two-phase production. Sample No. 9 also experienced early water breakthrough, a slow rise in water
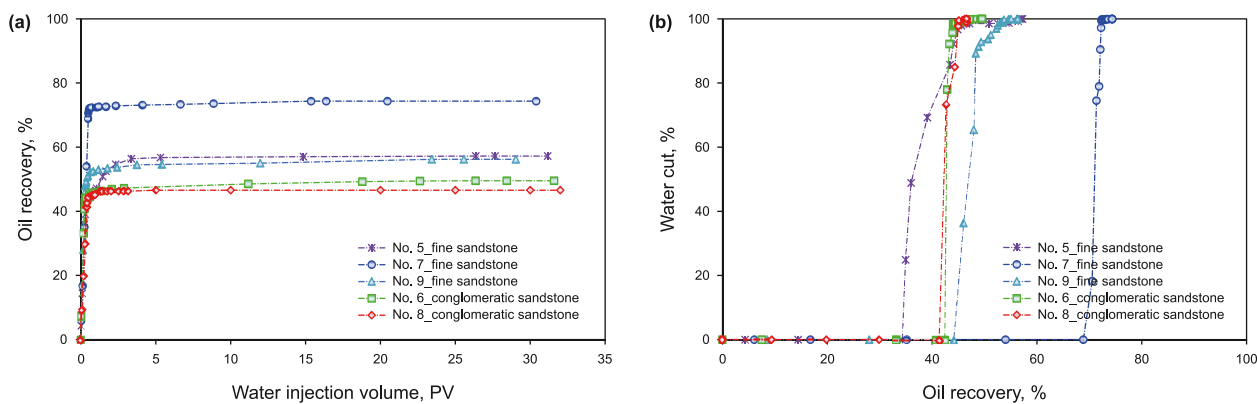
Fig. 11. Experimental results of water flooding. (**a**) Relationship between oil recovery and injection volume of water; (**b**) Relationship between water cut and oil recovery.
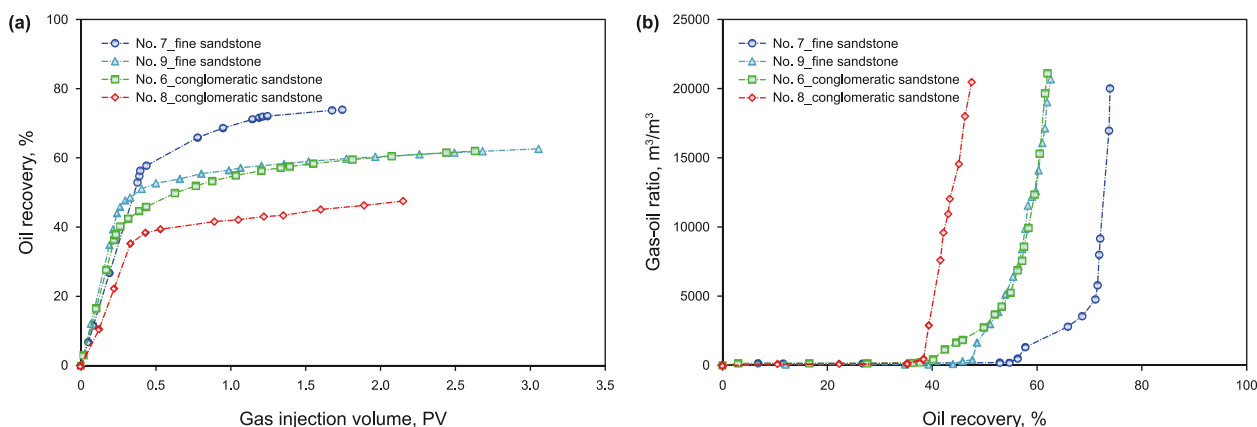

Fig. 12. Experimental results of gas flooding. (**a**) Relationship between oil recovery and injection volume of gas; (**b**) Relationship between gas−oil ratio and oil recovery.

cut, and broad two-phase production. On the other hand, sample No. 7 had late water breakthrough, a fast rise in water cut, and narrow two-phase production. Regarding gas flooding in Fig. 12(b), the conglomeratic sandstone samples reached gas breakthrough earlier compared to the fine sandstone samples. Sample No. 8, with the strongest reservoir heterogeneity, exhibited the fastest gas−oil ratio and the narrowest two-phase production. These differences in displacement characteristics can be attributed to the pore-throat characteristics of the different reservoirs as well as the combination of core samples. The former represents intralayer

heterogeneity, while the latter represents plane heterogeneity.

The evaluation results for gas and water flooding are presented in Table 5. The cumulative oil production contribution before water breakthrough was greater than that before gas breakthrough for the same samples. Following the water/gas breakthrough, the oil displacement efficiency during oil−water production was lower than that during oil−gas production for the same samples. When 1% of the original oil in place is produced during the two-phase production period, 0.08−0.19 pore volume (PV) of gas is required, which is significantly lower than the injection volume of water

Table 5
Evaluation results of gas and water flooding.

Core No.	Displacement type	Injection volume, PV	Final oil recovery, %	Oil recovery before water/gas breakthrough, %	Contribution of the cumulative oil production before water/gas breakthrough, %	Oil recovery during two-phase production, %	Injection volume when 1% original oil in place is produced during two-phase production, PV	I_p, mD/ (cP MPa)
5	Water flooding	26.36	57.2	34.9	61.0	22.3	1.17	129.13
7	Water flooding	16.37	74.4	70.6	94.9	3.8	3.91	41.77
9	Water flooding	23.42	56.2	46.0	81.8	10.2	2.26	4.44
6	Water flooding	26.35	49.5	42.9	86.6	6.7	3.92	240.63
8	Water flooding	2.02	46.6	42.7	91.6	3.9	0.43	47.85
7	Gas flooding	1.74	73.9	56.3	76.1	17.6	0.08	1152.52
9	Gas flooding	3.06	62.6	45.8	73.2	16.8	0.17	15.40
6	Gas flooding	2.63	62.0	40.2	64.8	21.8	0.11	1045.32
8	Gas flooding	2.15	47.5	38.4	80.7	9.2	0.19	287.10

(0.43–3.91 PV) required. Therefore, the oil production capacity during oil–gas production is stronger than that during oil–water production. Additionally, the seepage capacity of gas flooding was much greater than that of water flooding for the same samples. Based on the above analysis, it can be concluded that the development effect of gas flooding is superior to that of water flooding.

Sample Nos. 5, 7, and 9 are all fine sandstones. However, there were notable differences in the displacement characteristics between water and gas flooding, including oil displacement efficiency, water and gas breakthrough, water cut rise trend, and the gas–oil ratio. In terms of the pore-throat characteristics, the pore-throat sizes of sample Nos. 5 and 7 were larger compared to sample No. 9, and the pore-throat distributions of sample Nos. 7 and 9 were more concentrated than that of sample No. 5. Additionally, based on the core combination relationship presented in Tables 2 and 3, the ratios of maximum permeability to minimum permeability for sample Nos. 5, 7, and 9 were 7.7, 3.3, and 4.6, respectively. Consequently, the intralayer and plane heterogeneities of sample No. 5 are more pronounced than those of sample Nos. 7 and 9, resulting in a lower oil displacement efficiency for water flooding and an earlier water breakthrough for sample No. 5 compared to sample No. 7. Moreover, the lowest oil displacement efficiency observed for sample No. 9 during water flooding can be attributed to the inability of injected water to displace crude oil from small pore throats due to the poor reservoir quality and the large size of water molecules. However, when compared to water flooding, gas flooding can improve oil displacement efficiency by 6.4% for sample No. 9, indicating its potential in enhancing the development effect of low-permeability reservoirs. Sample No. 7, characterized by good homogeneity, exhibited a stable period of oil production capacity during the anhydrous period of water flooding, resembling piston displacement. Considering the advantages of gas flooding, it can be employed in homogeneous reservoirs to achieve a favorable development effect when there is an ample gas source and an appropriate tectonic angle.

According to the mercury intrusion pressure curves, conglomeratic sandstone exhibits stronger pore-throat heterogeneity compared to conventional sandstone, resulting in an earlier gas breakthrough earlier in Fig. 12(b). In Figs. 8 and 11, the seepage law and mercury intrusion pressure curves of sample No. 8 display four-stage characteristics, while those of sample No. 6 exhibit three-stage characteristics. Consequently, the heterogeneity of sample No. 8 is more pronounced than that of sample No. 6. This difference leads to significantly lower oil displacement efficiencies for gas and water flooding in sample No. 8 compared to sample No. 6. As the reservoir heterogeneity increases, gas channeling becomes more prominent, resulting in earlier gas breakthrough and a faster increase in the gas–oil ratio (Fig. 12(b)). Furthermore, the early water breakthrough observed in sample No. 5 can be attributed to strong plane heterogeneity. Therefore, reservoir heterogeneity is a crucial factor influencing displacement characteristics.

The strong heterogeneity of sample No. 8 results in more pronounced gas channeling compared to sample No. 6, leading to a smaller range of improvement in oil displacement efficiency (0.9%) by gas flooding in sample No. 8 compared to sample No. 6, which experienced a 12.5% improvement. While gas flooding can mitigate the impact of reservoir heterogeneity on the development effect, relying solely on a single energy supplementation mode may not achieve satisfactory results for strongly heterogeneous reservoirs. Therefore, further research is required to explore the optimal selection of energy supplementation modes to enhance the development of such reservoirs.

4.3.2. Enhancement of the development effect

To enhance the development effect of strongly heterogeneous reservoirs, we conducted associated gas flooding after water flooding in sample Nos. 5, 6, and 10. In this study, our study revealed that sample No. 5 had a ratio of maximum permeability to minimum permeability of 7.7, while sample No. 6 had a ratio of 9.5. Additionally, sample Nos. 8 and 10 served as parallel samples. Among the three samples, sample No. 5 exhibited strong plane heterogeneity, sample No. 6 had strong intralayer and plane heterogeneity, and sample No. 10 had the strongest intralayer heterogeneity. In the case of associated gas flooding after water flooding, we observed that the oil recovery of sample No. 5 was enhanced by 9.8% at a gas–oil ratio of 21,491 m^3/m^3. For sample No. 6, the oil recovery was enhanced by 18.0% at a gas–oil ratio of 21,814 m^3/m^3, which was 5.5% higher than the oil recovery achieved with gas flooding at a gas–oil ratio of 21,105 m^3/m^3. Sample No. 10 exhibited an oil recovery enhancement of 16.4% at a gas–oil ratio of 7097 m^3/m^3, demonstrating the best oil-increasing effect among the three samples at the same gas–oil ratio. Based on these findings, associated gas flooding after water flooding as a reasonable energy supplementation mode for enhancing the development of strongly heterogeneous reservoirs.

Based on the analysis of the seepage law, displacement characteristics, and associated gas flooding after water flooding for strongly heterogeneous reservoirs, several conclusions can be drawn: (1) The primary factor influencing the discontinuous and multistage seepage law in conglomeratic sandstone reservoirs is the unique characteristics of the multi-stage pore throats, including their size, proportion, distribution, number, and volume. Large pores and throats play a critical role in determining seepage capacity and oil displacement efficiency. (2) Oil production capacity during oil–gas production is stronger than that during oil–water production, and the seepage capacity of gas flooding surpasses that of water flooding. Therefore, gas flooding is a more effective method of energy supplementation for homogeneous reservoirs. However, reservoir heterogeneity significantly affects the displacement effects of water and gas flooding. A single energy supplementation mode cannot achieve satisfactory development outcomes for strongly heterogeneous reservoirs. (3) Associated gas flooding after water flooding emerges as a reasonable energy supplementation mode for enhancing the development effect of strongly heterogeneous reservoirs. Several reasons support this conclusion: (I) Gas molecules, due to their small size, can penetrate into small pore-throat spaces during displacement. (II) Water, occupying large pore throats, creates a "water lock" phenomenon after water flooding, slowing down the gas breakthrough and enabling more crude oil in small pore-throats to migrate towards larger pore throats under gas flooding. (III) Associated gas and crude oil exhibit partial miscibility, enhancing the mobility of the oil phase under formation temperature and pressure conditions.

In Fig. 13(a), several observations can be made: (1) The evaporation process causes a decrease in the content of C_7–C_{10} components in crude oil. (2) With an increasing injection volume of gas, the extraction of C_{11}–C_{19} components increases due to the influence of the extraction process. (3) The heavy components (C_{20}–C_{35}) exhibit a decrease, and they become the dominant components in the remaining oil. (4) In Fig. 13(b), the density of the produced oil decreases as the injection volume of gas increases. Based on the aforementioned analysis, it can be concluded that the miscibility of crude oil during the gas flooding process improves the quality of the produced oil.

In order to investigate the influence of injection volume, a displacement experiment using large-scale cores was conducted. The comprehensive changes in the composition of the produced oil are presented in Fig. 14, and the trends observed in the variation of produced oil components when the injection volume is less than 5 PV are consistent with those shown in Fig. 13(a). However, as the injection volume continues to increase, there is a decrease in the
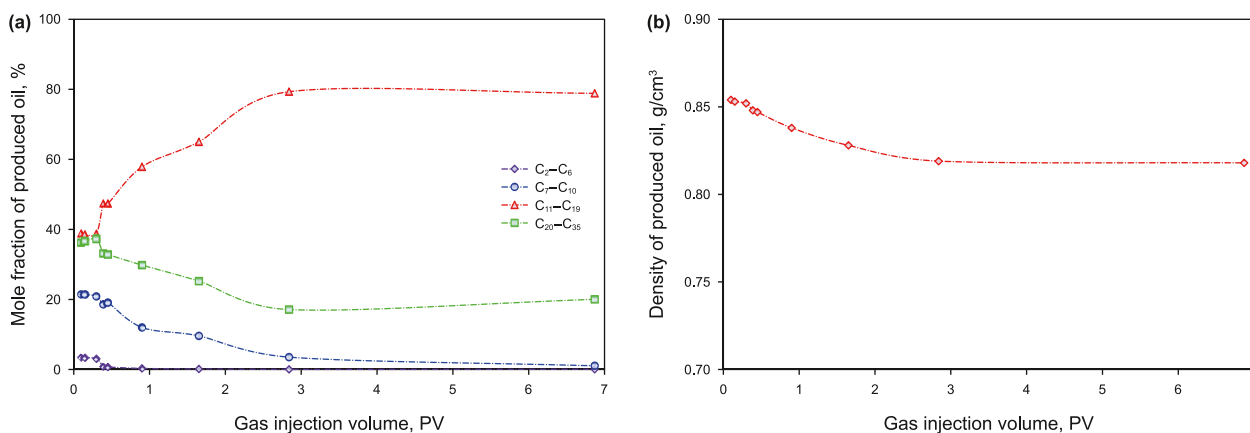
Fig. 13. Changes in composition (**a**) and density (**b**) of the produced oil during gas flooding.
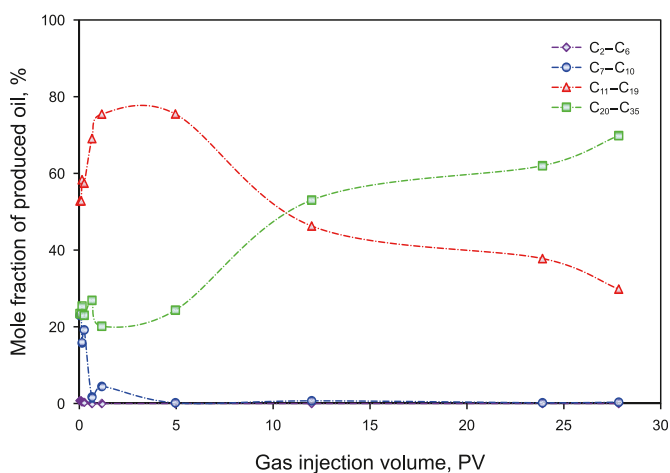

Fig. 14. Changes in composition of produced oil in the gas flooding process of large-scale cores.

proportion of light components in the produced oil, accompanied by an increase in the proportion of heavy components. It should be noted that achieving an injection volume of more than 5 PV during oilfield development with gas flooding can be challenging. Gas flooding has the ability to remove light components from the reservoir, leaving behind heavy components. This phenomenon can lead to the deposition of solids and a reduction in the physical properties of the reservoir.

The solution gas−oil ratio in the LSG Formation of the BBW Basin typically reaches up to approximately 100 m³/m³, indicating the presence of abundant associated gas resources. However, due to production facility limitations, a significant amount of associated gas cannot be sold and is instead flared through "torch" burning. In the initial stages of oilfield development for strongly heterogeneous reservoirs in the LSG Formation, water flooding is employed. As the reservoir enters the middle-high water cut stage, the energy supplement mode is transitioned to associated gas flooding to enhance the development effect. This approach aims to optimize the utilization of the available associated gas resources and maximize the recovery of oil from the reservoir.

5. Conclusions

The differences in the pore-throat among different reservoirs were studied by conducting numerous microscopic pore-throat

experiments. Additionally, four samples with short cores, five samples with combined long cores, and one sample with a whole-diameter core were tested with different flooding systems, to investigate the seepage characteristics and determine reasonable energy supplement modes for these reservoirs. The conclusions drawn are as follows.

(1) Conglomeratic sandstone exhibits larger pores and throats, a higher proportion of macropores, a smaller number and volume of effective throats per unit pore volume, wider distribution and stronger discontinuity of the pores and throats, as well as stronger heterogeneity compared to conventional sandstone. Under similar reservoir permeability, conglomeratic sandstone exists more multistage pore-throat structure and multistage seepage than conventional sandstone, by utilizing capillary pressure model and two-phase seepage model. Moreover, the multistage seepage is completely consistent with multistage pore-throat structure.

(2) The seepage capacities of oil−gas flow were found to be 3.5 to 27.6 times higher than those of oil−water flow for the same samples, primarily due to the small size of gas molecules and the miscibility between associated gas and crude oil. Additionally, the associated gas can enter the small pore-throat spaces in the displacement process, resulting in improved oil displacement efficiency.

(3) The oil-displacement efficiencies achieved through associated gas flooding after water flooding are found to be enhanced by 7.3%−16.4%, compared to water flooding alone, at a gas−oil ratio of approximately 7000 m³/m³. As the reservoir heterogeneity increases, the oil displacement efficiency also increases. Therefore, it is determined that associated gas flooding after water flooding is a better mode compared to a single mode of energy supplementation for strongly heterogeneous sandstone reservoirs.

It is important to note that this paper solely analyzes and demonstrates the selection of reasonable energy supplement modes for different reservoirs within the LSG Formation in the BBW Basin from an experimental perspective. A systematic research process, from experimentation to oilfield application, is required. Subsequently, the rational development modes of different reservoirs will be further discussed from the perspective of oilfield development. This includes examining the timing of associated gas flooding, alternations between water and gas, changes in miscibility pressure during gas flooding, and other relevant factors. The aim is to promote the efficient development of highly

heterogeneous reservoirs within the LSG Formation in the BBW Basin.

CRediT authorship contribution statement

Lei Wang: Conceptualization, Data curation, Methodology, Writing − original draft, Writing − review & editing, Formal analysis, Investigation. **Xiao Lei:** Resources, Supervision. **Qiao-Liang Zhang:** Project administration, Resources, Funding acquisition. **Guang-Qing Yao:** Supervision. **Bo Sui:** Visualization. **Xiao-Jun Chen:** Writing − review & editing. **Ming-Wei Wang:** Formal analysis. **Zhen-Yu Zhou:** Validation. **Pan-Rong Wang:** Visualization. **Xiao-Dong Peng:** Software.

Declaration of competing interest

The author has no relevant financial or non-financial interests to disclose. There is no conflict of interest to publish this work in this journal.

Acknowledgment

References

Akin, S., Kovscek, A., 1999. Imbibition studies of low-permeability porous media. In: Western Regional Meeting Held in Anchorage, Alaska. https://doi.org/10.2118/54590-MS.

Alamooti, A.M., Ghazanfari, M.H., Masihi, M., 2018. Investigating the relative permeability behavior in presence of capillary effects in composite core systems. J. Petrol. Sci. Eng. 160, 341—350. https://doi.org/10.1016/j.petrol.2017.10.051.

Babadagli, T., Hatiboglu, C.U., Hamida, T., 2005. Evaluation of matrix-fracture transfer functions for counter-current capillary imbibition. In: SPE Asia Pacific Oil & Gas Conference and Exhibition. https://doi.org/10.2118/92111-MS.

Cai, J., San José Martínez, F., Martín, M.A., et al., 2015. An introduction to flow and transport in fractal models of porous media: Part II. Fractals 23 (1), 1502001. https://doi.org/10.1142/S0218348X15020016.

Cai, J., Hu, X., Xiao, B., et al., 2017. Recent developments on fractal-based approaches to nanofluids and nanoparticle aggregation. Int. J. Heat Mass Transfer 105, 623—637. https://doi.org/10.1016/j.ijheatmasstransfer.2016.10.011.

Chen, H., Liu, X., Zhang, C., et al., 2022. Effects of miscible degree and pore scale on seepage characteristics of unconventional reservoirs fluids due to supercritical CO_2 injection. Energy 239, 122287. https://doi.org/10.1016/j.energy.2021.122287.

Chen, X., Yao, G., Cai, J., et al., 2017. Fractal and multifractal analysis of different hydraulic flow units based on micro-CT images. J. Nat. Gas Sci. Eng. 48, 145—156. https://doi.org/10.1016/j.jngse.2016.11.048.

Dou, H.E., 2013. Discussion on 'Is a starting pressure gradient necessary for flow in porous media?'. Acta Pet. Sin. 34 (2), 412—416. https://doi.org/10.7623/syxb201302028 (in Chinese).

Esmaeili, S., Sarma, H., Harding, T., et al., 2019. A data-driven model for predicting the effect of temperature on oil-water relative permeability. Fuel 236, 264—277. https://doi.org/10.1016/j.fuel.2018.08.109.

Fatemi, S.M., Sohrabi, M., Jamiolahmady, M., et al., 2011. Experimental investigation of near-miscible water-alternating-gas (WAG) injection performance in water-wet and mixed-wet systems. In: Offshore Europe Oil and Gas Conference and Exhibition. https://doi.org/10.2118/145191-MS.

Gao, H., Li, H.A., 2016. Pore structure characterization, permeability evaluation and enhanced gas recovery techniques of tight gas sandstones. J. Nat. Gas Sci. Eng. 28, 536—547. https://doi.org/10.1016/j.jngse.2015.12.018.

Guo, P., Li, S.-L., Du, Z.-M., 2002. Evaluation on IOR by gas injection in low permeability oil reservoir. J. Southwest Petrol. Univ. (Sci. Technol. Ed.) 24 (5), 46—50. https://doi.org/10.3863/j.issn.1000-2634.2002.05.015 (in Chinese).

Guo, P., Luo, Y.-Q., He, J.-L., et al., 2003. A feasibility study of gas injection for oil

reservoirs after waterflooding. J. Southwest Petrol. Univ. (Sci. Technol. Ed.) 25 (4), 37—40. https://doi.org/10.1007/BF02974893 (in Chinese).

He, H., Zhou, Y.-Q., Long, W.-J., et al., 2021. Pore throat microstructures of low-ultra-low permeability reservoirs and their influence on water displacement characteristics: taking the Chang 3 reservoir of Weibei Oilfield in Ordos Basin as an example. Petrol. Geol. Recovery Effic. 28 (4), 23—34. https://doi.org/10.13673/j.cnki.cn37-1359/te.2021.04.003.

Høgnesen, E.J., Standnes, D.C., Austad, T., 2004. Scaling spontaneous imbibition of aqueous surfactant solution into preferential oil-wet carbonates. Energy Fuels 18 (6), 1665—1675. https://doi.org/10.1021/ef040035a.

Honarpour, M., Mahmood, S., 1988. Relative-permeability measurements: an overview. J. Petrol. Technol. 40 (8), 963—966. https://doi.org/10.2118/18565-PA.

Iyi, D., Balogun, Y., Oyeneyin, B., et al., 2022. A numerical study of the effects of temperature and injection velocity on oil-water relative permeability for enhanced oil recovery. Int. J. Heat Mass Transfer 191, 122863. https://doi.org/10.1016/j.ijheatmasstransfer.2022.122863.

Jiang, P., Zhang, H., Wang, L., et al., 2021. An evaluation method of reservoir "sweet spots" in low permeability oilfields of Beibuwan Basin. Acta Pet. Sin. 42 (6), 751—764. https://doi.org/10.7623/syxb202106005 (in Chinese).

Ju, Y., Gong, W., Chang, W., et al., 2020. Effects of pore characteristics on water-oil two-phase displacement in non-homogeneous pore structures: a pore-scale lattice Boltzmann model considering various fluid density ratios. Int. J. Eng. Sci. 154, 103343. https://doi.org/10.1016/j.ijengsci.2020.103343.

Kate, J.M., Gokhale, C.S., 2006. A simple method to estimate complete pore size distribution of rocks. Eng. Geol. 84, 48—69. https://doi.org/10.1016/j.enggeo.2005.11.009.

Katz, A.J., Thompson, A., 1985. Fractal sandstone pores: implications for conductivity and pore formation. Phys. Rev. Lett. 54 (12), 1325—1328. https://doi.org/10.1103/PhysRevLett.54.1325.

Krohn, C.E., 1988. Sandstone fractal and Euclidean pore volume distributions. J. Geophys. Res. Solid Earth 93 (B4), 3286—3296. https://doi.org/10.1029/JB093iB04p03286.

Kulkarni, M.M., 2005. Multiphase mechanisms and fluid dynamics in gas injection enhanced oil recovery processes. PhD Dissertation. Louisiana State University and Agricultural & Mechanical College.

Li, C.-L., Yang, Y.-Q., 2008. There is not a starting pressure gradient in low-permeability reservoirs at all. J. Southwest Petrol. Univ. (Sci. Technol. Ed.) 30 (3), 167—170. https://doi.org/10.3863/j.issn.1000-2634.2008.03.043 (in Chinese).

Li, K., 2010. Analytical derivation of Brooks−Corey type capillary pressure models using fractal geometry and evaluation of rock heterogeneity. J. Petrol. Sci. Eng. 73 (1—2), 20—26. https://doi.org/10.1016/j.petrol.2010.05.002.

Li, K., Horne, R.N., 2001. Characterization of spontaneous water imbibition into gas-saturated rocks. SPE J. 6 (4), 375—384. https://doi.org/10.2118/74703-PA.

Li, K., Horne, R.N., 2005a. An analytical model for production decline-curve analysis in naturally fractured reservoirs. SPE Reserv. Eval. Eng. 8 (3), 197—204. https://doi.org/10.2118/83470-PA.

Li, K., Horne, R.N., 2005b. Computation of capillary pressure and global mobility from spontaneous water imbibition into oil-saturated rock. SPE J. 10 (4), 458—465. https://doi.org/10.2118/80553-PA.

Li, K., Horne, R.N., 2006. Generalized scaling approach for spontaneous imbibition: an analytical model. SPE Reserv. Eval. Eng. 9 (3), 251—258. https://doi.org/10.2118/77544-PA.

Li, K., Horne, R.N., 2007. Comparison and verification of production prediction models. J. Petrol. Sci. Eng. 55 (3—4), 213—220. https://doi.org/10.1016/j.petrol.2006.08.015.

Lian, T.L., Radhakrishnan, P., Daya Sagar, B.S., 2004. Morphological decomposition of sandstone pore−space: fractal power-laws. Chaos, Solit. Fractals 19 (2), 339—346. https://doi.org/10.1016/S0960-0779(03)00046-8.

Liu, L., Dai, S., Ning, F., et al., 2019. Fractal characteristics of unsaturated sands−implications to relative permeability in hydrate-bearing sediments. J. Nat. Gas Sci. Eng. 66, 11—17. https://doi.org/10.1016/j.jngse.2019.03.019.

Liu, W.-X., Cheng, Q.-Q., Wang, Y.-B., et al., 2006. Micro-analysis and its application of oil and gas reservoir characteristics. Petrol. Geol. Exp. 28 (5), 489—492. https://doi.org/10.11781/sysydz200605489 (in Chinese).

Liu, W., Xiao, Z.-X., Yang, S.-Y., et al., 2009. Comparative studies on methods of evaluation of reservoir pore structure by using NMR (nuclear magnetic resonance) well logging data. Oil Geophys. Prospect. 44 (6), 773—778. https://doi.org/10.13810/j.cnki.issn.1000-7210.2009.06.018 (in Chinese).

Liu, X., Chen, H., Chen, Z., et al., 2024. Study on characterization and distribution of four regions of tight sandstone condensate gas reservoirs in the depletion development process. Fuel 358, 130267. https://doi.org/10.1016/j.fuel.2023.130267.

Liu, Z., Li, Y., Leng, R., et al., 2020. Effects of pore structure on surfactant/polymer flooding-based enhanced oil recovery in conglomerate reservoirs. Petrol. Explor. Dev. 47 (1), 134—145. https://doi.org/10.1016/S1876-3804(20)60012-X.

Mirzaei-Paiaman, A., Saboorian-Jooybari, H., Chen, Z., et al., 2019. New technique of true effective mobility (TEM-Function) in dynamic rock typing: reduction of uncertainties in relative permeability data for reservoir simulation. J. Petrol. Sci. Eng. 179, 210—227. https://doi.org/10.1016/j.petrol.2019.04.044.

Nguyen, V.H., Sheppard, A.P., Knackstedt, M.A., et al., 2006. The effect of displacement rate on imbibition relative permeability and residual saturation. J. Petrol. Sci. Eng. 52 (1—4), 54—70. https://doi.org/10.1016/j.petrol.2006.03.020.

Nurkamelia, Arihara, N., 2004. Analysis of spontaneous capillary imbibition for improved oil recovery. In: SPE Asia Pacific Oil & Gas Conference and Exhibition.

https://doi.org/10.2118/88498-MS.

Pang, Z.-Y., Li, Y., Duan, W., et al., 2017. Classification and characterization of microscopic pore structures in low and extra-low permeability reservoirs: a case study of reservoirs Chang 2 and Chang 6 in Yanchang Formation of Yanchang Oilfield. Xinjing Pet. Geol. 38 (2), 193–197. https://doi.org/10.7657/XJPG20170213 (in Chinese).

Ramstad, T., Berg, C.F., Thompson, K., 2019. Pore-scale simulations of single-and two-phase flow in porous media: approaches and applications. Transport Porous Media 130 (1), 77–104. https://doi.org/10.1007/s11242-019-01289-9.

Saafan, M., Ganat, T., Mohyaldinn, M., et al., 2022. A fractal model for obtaining spontaneous imbibition capillary pressure curves based on 2D image analysis of low-permeability sandstone. J. Petrol. Sci. Eng. 208, 109747. https://doi.org/10.1016/j.petrol.2021.109747.

Tavassoli, Z., Zimmerman, R.W., Blunt, M.J., 2005. Analysis of counter-current imbibition with gravity in weakly water-wet systems. J. Petrol. Sci. Eng. 48 (1–2), 94–104. https://doi.org/10.1016/j.petrol.2005.04.003.

Wang, L., Liu, C., Jiang, P., et al., 2019a. Characterization of two-phase flow in porous media using global mobility. J. Petrol. Sci. Eng. 177, 188–197. https://doi.org/10.1016/j.petrol.2019.02.050.

Wang, L., Zhang, H., Peng, X., et al., 2019b. Water-sensitive damage mechanism and injection water source optimization of low permeability sandy conglomerate reservoirs. Petrol. Explor. Dev. 46 (6), 1148–1158. https://doi.org/10.1016/S1876-3804(19)60275-2.

Wang, L., Chen, X.J., Zhang, H., et al., 2023. A new index to evaluate the seepage capacity of water-wet sandstone reservoirs. J. Energy Eng. 149 (4), 04023018. https://doi.org/10.1061/JLEED9.EYENG-4780.

Xiao, Q., Yang, Z., Wang, Z., et al., 2020. A full-scale characterization method and application for pore-throat radius distribution in tight oil reservoirs. J. Petrol. Sci. Eng. 187, 106857. https://doi.org/10.1016/j.petrol.2019.106857.

Yin, S.-L., Chen, G.-Y., Chen, Y.-K., et al., 2019. Mechanism of complex modes of the pore structure of sandstone/conglomerate reservoirs. J. Southwest Petrol. Univ. (Sci. Technol. Ed.) 41 (1), 1–17. https://doi.org/10.11885/j.issn.1674-5086.2018.01.01.01 (in Chinese).

Yu, B., Cheng, P., 2002. A fractal permeability model for bi-dispersed porous media. Int. J. Heat Mass Transfer 45 (14), 2983–2993. https://doi.org/10.1016/S0017-9310(02)00014-5.

Zeng, L., Qi, J., Li, Y., 2007. The relationship between fractures and tectonic stress field in the extra low-permeability sandstone reservoir at the south of western Sichuan depression. J. China Univ. Geosci. 18 (3), 223–231. https://doi.org/10.1016/S1002-0705(08)60003-5.

Zhang, D.-W., Chen, F.-J., Cheng, G., 2006. The microscopic features of pore structure in Gaotaizi oil layer of Daqingzijing area. Oil Geol. 27 (5), 668–674. https://doi.org/10.3321/j.issn:0253-9985.2006.05.012 (in Chinese).

Zhang, X.-W., Guo, H.-K., Li, H.-B., 2018. Experimental study on imbibition oil displacement of tight oil reservoir using NMR technology. Bull. Sci. Technol. 34 (8), 35–40. https://doi.org/10.13774/j.cnki.kjtb.2018.08.007 (in Chinese).

Zhao, M.-g., Zhou, H.-f., Chen, D.-f., 2008. Investigation and application on gas-drive development in ultra-low permeability reservoirs. J. Hydrodyn. 20 (2), 254–260. https://doi.org/10.1016/S1001-6058(08)60054-2.

Zhu, H., Zhang, T., Zhong, D., et al., 2019. Binary pore structure characteristics of tight sandstone reservoirs. Petrol. Explor. Dev. 46 (6), 1297–1306. https://doi.org/10.1016/S1876-3804(19)60283-1.